Journal Pre-proofs

Plasma-assisted highly dispersed Pt single atoms on Ru nanoclusters electrocatalyst for pH-universal hydrogen evolution

Yanjun Chen, Jing Li, Ning Wang, Yanan Zhou, Jian Zheng, Wei Chu

PII: S1385-8947(22)03098-4
DOI: https://doi.org/10.1016/j.cej.2022.137611
Reference: CEJ 137611

To appear in: *Chemical Engineering Journal*

Received Date: 11 May 2022
Revised Date: 10 June 2022
Accepted Date: 15 June 2022

Please cite this article as: Y. Chen, J. Li, N. Wang, Y. Zhou, J. Zheng, W. Chu, Plasma-assisted highly dispersed Pt single atoms on Ru nanoclusters electrocatalyst for pH-universal hydrogen evolution, *Chemical Engineering Journal* (2022), doi: https://doi.org/10.1016/j.cej.2022.137611

Plasma-assisted highly dispersed Pt single atoms on Ru nanoclusters electrocatalyst for pH-universal hydrogen evolution

Yanjun Chen [a,‡], Jing Li [b,*], Ning Wang [c], Yanan Zhou [a,*], Jian Zheng [a], Wei Chu [a,*]

[a] *Department of Chemical Engineering, Sichuan University, Chengdu 610065, China*

[b] *Department of Chemistry, Tsinghua University, Beijing 100084, China*

[c] *Faculty of Environment and Life, Beijing University of Technology, Beijing, 100124 China*

* Corresponding author at: Department of Chemical Engineering, Sichuan University, Chengdu 610065, China

E-mail address: lijing93@mail.tsinghua.edu.cn (Jing Li); yananzhou@163.com (Yanan Zhou); chuwei1965@scu.edu.cn (Wei Chu)

Abstract

Exploring highly active and stable electrocatalyst using trace noble metals for hydrogen evolution reaction (HER) is urgently needed but still challenging. Here, atomically dispersed Pt on ultrafine Ru nanoclusters (~1.46 nm) loaded by the commercial acetylene black (Acet) support is fabricated by a facile one-step cold-plasma technique. The Pt single atoms on Ru nanoclusters electrocatalyst ($Pt_{0.47}$-Ru/Acet) with 0.47 wt% content of Pt exhibit an excellent HER activity in all pH, achieving ultralow overpotential of only 17, 28, and 8 mV at 10 $mA \cdot cm^{-2}$ in 1 M KOH, 0.5 M H_2SO_4, and 1 M PBS, respectively. And the mass activity of $Pt_{0.47}$-Ru/Acet catalyst in alkaline is about 5.54 and 2.15 times that of commercial Ru/C and Pt/C catalyst at an overpotential of 100 mV, respectively. Meanwhile, after 8000 CV cycles, there is barely performance decrease for $Pt_{0.47}$-Ru/Acet, displaying good stability. DFT calculation reveals that the Pt single atoms could effectively regulate the electronic structure of Ru clusters, and reduce the energy barriers of water dissociation (Volmer step) as well as subsequent hydrogen evolution (Heyrovsky step), thus enhancing the alkaline HER performance effectively. This work provides an effective approach to designing a high-performance HER electrocatalyst with the atomic-dimension Pt surface modification.

Keywords: Plasma, Pt single atoms, Ru nanoclusters, Pt-Ru/Acet, pH-universal hydrogen evolution

1. Introduction

The aggravation of global energy shortage and environmental pollution drive researchers to explore sustainable and renewable clean fuels. Hydrogen has become the most promising alternative to fossil fuels due to its high energy density and green combustion products [1]. Recently, hydrogen evolution from electrochemical water splitting has aroused increasing attention because it is promising to produce non-polluted "green hydrogen" instead of "gas-reforming hydrogen" with massive carbon emissions [2-6]. However, the bottleneck for large-scale hydrogen production via water splitting is severely impeded by its high cost (~ \$5 kg^{-1}/H_2) versus gas reforming (~ \$1.4 kg^{-1}/H_2) [7]. Thereinto, as one of the keys to water splitting, catalysts should be elaborately designed since they determined the (i) electricity input during water splitting and (ii) their spending in preparation and material costs. In this regard, two basic requirements of the next-generation catalysts should be met to control the cost at a reasonable level: (i) high activity to allow lower overpotential/cell voltage thus lower electricity consumption; (ii) decreasing the dosage of the noble metals (Pt and Ru) due to their limited reserves and high price. Although some non-precious metal electrocatalysts have been developed for hydrogen evolution, their HER performances are still inferior to that of precious metal-based catalysts [8]. Other aspects, such as facile and scalable preparation method, long operation durability, and pH-universality, are also necessary to minimize the operation costs. Yet, electrocatalysts endowed with all-above features have not been well exploited.

Currently, Ru and Pt stand for the most active catalysts in basic and acid solutions for hydrogen evolution reaction (HER), respectively [9, 10]. While in alkaline and neutral electrolytes, the reaction kinetics is about two orders of magnitude lower than that in acid due to the sluggish water dissociation ($H_2O + e^- \rightarrow H^* + OH^-$, Volmer step), leading to large HER overpotential [11-13]. Even for representative Ru catalysts, the fracture ability of the H-OH bond (*i.e.*, water dissociation) is still not ideal [14, 15]. Therefore, research that improves the intrinsic activity and lowers the barrier of water dissociation of Ru-based catalyst is still under exploration. Many efforts, such as dual-metal RuRh [16], Pd_3Ru [17], RuIr [18],

RuCo [19-21], RuCu [22], RuMo [23], and PtRu [24, 25] electronic structure engineering, surface strain have been done to further reduce the overpotential and improve the HER activity [3, 26-30]. Nevertheless, most of these catalysts either suffer from high noble metal dosage or can only work under alkaline solution with large overpotential. Recently, some reports have revealed that a single-atom tailoring strategy for metal-based catalysts can not only regulate the local electronic structure, improving the intrinsic activity, but also maintain a high electrochemically active surface area [31-33]. For example, Li et.al created single-atom nickel modified Pt nanowires by using a partial electrochemical dealloying approach, which has abundant activated Pt sites next to single-atom nickel and minimal blockage of the surface Pt sites, exhibiting an excellent activity for the hydrogen evolution [31]. Besides the intrinsic activity improvement, another approach to enhancing the HER performance is exposing more active sites of the Ru catalysts [34]. Therefore, downsizing Ru active species is significant because a smaller size (such as nanoclusters) can afford more exposed active sites than that provided by larger nanoparticles at a given metal load [35]. Nevertheless, conventional methods (annealing and solvothermal) usually lead to Ru particle aggregation with an average size larger than 3 nm due to the high surface energy during thermal treatment, which poses a contradiction between high HER performance and low Ru content [36-39]. In our previous work, we have demonstrated that the cold-plasma technique could effectively solve this dilemma. Plasma contains various high-energy fragments, like electrons, ions, radicals, *etc*. Particularly, high temperature is exempt in a cold plasma, where the whole plasma jet is close to room temperature but the high-energy electrons have a strong ability to reduce metal ions [40]. Consequently, the aggregation of the electron-reduced nuclei can be effectively inhibited benefiting from the rapid nucleation of metal ions and slow crystal growth. As a result, the metals synthesized by plasma treatment show higher dispersion and expose more active sites than those by the conventional heat treatment method. Based on this theorem, we have successfully synthesized a set of single-atom catalysts (such as Pt, Pd, Cu, Co) [41, 42] and small-sized nanocatalysts [43, 44] with high dispersion previously.

Therefore, it is expected to exploit an electrocatalyst comparable or even superior to commercial Pt and Ru nanocatalysts with minimum noble metal content.

In this work, highly dispersed Ru-based nanocluster electrocatalysts (~1.46 nm) were developed based on the cold-plasma technique. Encouragingly, atomically Pt modified Ru nanoclusters exhibited multi-functionality in all-pH HER. The $Pt_{0.47}$-Ru/Acet catalyst presents an outstanding HER performance with a low overpotential of 17, 28, and 8 mV at 10 $mA \cdot cm^{-2}$ in 1 M KOH, 0.5 M H_2SO_4, and 1 M PBS, respectively, which are superior to those of monometallic counterparts and commercial Pt/C as well as most previously Pt or Ru nanocatalysts with higher content. Meanwhile, the mass activity of $Pt_{0.47}$-Ru/Acet catalyst in alkaline is about 5.54 and 2.15 times better than that of commercial Ru/C and 20 wt% Pt/C catalysts at an overpotential of 100 mV, respectively, and the $Pt_{0.47}$-Ru/Acet catalyst exhibits good stability and regenerative property. Density functional theory (DFT) simulations demonstrate that the introduction of single atoms Pt on the Ru nanoclusters surface could modulate the electronic structure of Ru, decreasing the water dissociation energy and subsequent energy barrier of hydrogen evolution, thus leading to excellent HER performance. Additionally, $Pt_{0.47}$-Ru/Acet catalyst also presents bifunctionality in both HER and OER and thus can be well adapted in assembled two-electrode overall water splitting system.

2. Experiment section

2.1 Materials

Ruthenium trichloride ($RuCl_3 \cdot H_2O$, Aladdin, 98%), chloroplatinic acid ($H_2PtCl_6 \cdot xH_2O$, Adamas, 98%), acetylene black (Tianjin Yiborui Chemical Co., Ltd.), Nafion (Dupont, 5 wt%), Potassium hydroxide (KOH), sulphuric acid (H_2SO_4, 95–98%) and ethanol (EtOH) were purchased from Chengdu Kelon Chemical Reagent Co., Ltd.. Nickel foam (1.7mm) was purchased from Changde Liyuan New Material Co., Ltd. and further treated with hydrochloric acid (HCl, 3M) and ethanol.

2.2 Materials Synthesis

2.2.1 Synthesis of Pt-Ru/Acet

The synthesis procedure of $Pt_{0.47}$-Ru/Acet catalyst was as follows: 100 mg

acetylene black (Acet) was dispersed in 5 mL absolute ethanol including 1.18 mL $RuCl_3 \cdot H_2O$ (0.041 M) and 0.51 mL $H_2PtCl_6 \cdot xH_2O$ (0.01 M), and then the above-mixed solution was ultrasonic of 60 min to obtain uniform dispersion. Subsequently, the dispersion solution was evaporated and dried at 60°C. After grinding the dried black solid into a fine powder, taking 20 mg of the powder was processed by the glow discharge plasma technology under a nitrogen atmosphere with a flow rate of 20 mL/min, and the power was 80 W. The obtained product was $Pt_{0.47}$-Ru/Acet catalyst. Furthermore, Pt_x-Ru/Acet (x=0.11, 0.15, 0.21, 2.04， x is Pt weight percentage) catalysts with different Pt content were prepared by adding the variable volumes of $H_2PtCl_6 \cdot xH_2O$ such as 0.13 mL, 0.26 mL, 0.38 mL, 2.56 mL. And the Pt weight percentage was evaluated via inductively coupled plasma-optical emission spectrometry (ICP-OES, Table S1).

2.2.2 Synthesis of Ru/Acet, Ru/Acet-Calc, and Pt/Acet

The preparation process of Ru/Acet, Ru/Acet-Calc, and Pt/Acet samples was similar to that of Pt-Ru/Acet, but for Ru/Acet except that no $H_2PtCl_6 \cdot xH_2O$ (0.01 M) was added. For Ru/Acet-Calc, a calcination procedure under a nitrogen atmosphere at 500°C for 2h was used instead of plasma technology. For Pt/Acet with diverse Pt content was obtained without the adding of $RuCl_3 \cdot H_2O$ (0.041 M).

2.3 Material Characterizations

The morphology of the catalyst was characterized by a high-angle annular dark-field scanning transmission electron microscope (HAADF-STEM) and energy-dispersive X-ray spectroscopy (EDS) elemental mapping which was performed on an FEI Titan 80-300 microscope working at 200 kV. X-ray photoelectron spectroscopy (XPS) was obtained on Thermo Scientific K-Alpha, and all data were corrected with carbon calibration at 284.8 eV. X-ray diffraction (XRD) patterns were carried out on a PANalytcal X'Pert PRO equipment with Cu-Kα radiation (λ=1.5418 Å, 45 kV, 40mA) in the 2θ range from 10° to 90° at $5°min^{-1}$. Inductively coupled plasma-optical emission spectrometry (ICP-OES) was conducted on Agilent 720ES. The X-ray absorption fine structure spectra (XAS) of Pt at L_3-edge and Ru at K-edge were separately collected at the beamlines of TLS07A1 and TPS44A1 at National

Synchrotron Radiation Research Center (NSRRC), Taiwan.

2.4 Electrochemical measurements

Electrochemical performances of all samples were conducted on CHI 660E electrochemical workstation with a typical three-electrode cell device in 1 M KOH electrolyte under a constant temperature of 25 ℃. The platinum plate was the counter electrode and Hg/HgO electrode was used as the reference electrode. Nickel foam (1×1 cm^2) coated with catalyst dispersion was used as the working electrode, and the specific preparation method was as follows: 5 mg electrocatalyst was ultrasonically dispersed in 500 μL mixed solution containing 25 μL Nafion (Dupont, 5 wt%) and 475 μL ethanol to form a homogeneous ink. Subsequently, 200 μL of the ink was dropped onto the nickel foam (1×1 cm^2) and dried. Before the electrochemical test, the Hg/HgO reference electrode was calibrated in 1 M KOH electrolyte with saturated H_2 (Figure S1). And all potentials were converted into the reversible hydrogen electrode (RHE) as the following equation: $E_{vs.\ RHE} = E_{vs.\ Hg/HgO} + 0.923$ V.

The polarization curves were obtained by linear sweep voltammetry (LSV) measurements with a scan rate of 10 $mV \cdot s^{-1}$ and all data in this wok were corrected with iR compensation by measuring the resistance of an uncompensated solution via EIS. And the HER activity of the as-prepared catalyst was evaluated via overpotential (η_{10}) at a current density of 10 $mA \cdot cm^{-2}$. The overall water splitting was carried out by a two-electrode cell with a scan rate of 10 $mV \cdot s^{-1}$ in 1 M KOH electrolyte. The electrochemical impedance spectroscopy (EIS) was conducted at an overpotential of 50 mV with a frequency from 0.1 to 10^5 Hz. The stability measurements were investigated by chronopotentiometry (*i-t* curves at the current density of 20 $mA \cdot cm^{-2}$) and cyclic voltammetry (CV) scanning for 8000 cycles with a sweep rate of 50 $mV \cdot s^{-1}$.

3. Results and discussion

3.1 Morphology and structure characterizations

To start, Ru/Acet-Calc via conventional calcination method was prepared for comparison. From TEM and STEM images (Figure S2 and S3), Ru/Acet via plasma approach shows a much smaller size (~1.41 nm) than that of Ru/Acet-Calc (~7.32

nm), indicating the significantly higher dispersion of Ru/Acet. Likewise, highly dispersed Pt-Ru/Acet catalysts with various Pt content were synthesized by this facile cold-plasma method. As illustrated in **Scheme 1**, the Ru^{3+} and $PtCl_6^{2-}$ ions were co-absorbed on the Acet support via wet impregnation. Then, the dried precursor powder was subsequently placed in a porcelain boat and exposed under N_2 plasma. In this procedure, the high-energy electrons with strong reducibility in ionized nitrogen plasma transfer to metal cations, promoting the co-reduction and nucleation of metal species. Meanwhile, the whole plasma jet is close to room temperature, thus the aggregation of the electron-reduced nuclei can be effectively inhibited benefiting from the rapid nucleation of metal ions and slow crystal growth [40]. Consequently, the highly dispersed Pt single atoms modified Ru nanoclusters anchored on Acet support electrocatalyst (Pt-Ru/Acet) can be in-situ fabricated by N_2 cold-plasma treatment. The metal size distribution of the catalysts was calculated based on the STEM images (Figure 1a, b and Figure S4, 5). With the increase of Pt content from 0.11 to 2.04 wt%, the average size of Pt-Ru/Acet shows a slight increase from 1.43 to 2.25 nm (Figure 1c and Figure S4, 5). For our optimized sample, $Pt_{0.47}$-Ru/Acet catalyst only has a small cluster size of ~1.46 nm. Further from the XRD spectra of catalysts in Figure S6, it can be seen that no crystallized metallic phase (Ru or Pt) is observed in all catalysts except for the characteristic peaks of Acet (25.6° and 43.3°), indicating that the metal species are highly dispersed in the catalyst. The distribution of Pt atoms was further characterized by HAADF-STEM. As shown in Figure 1d, the atomically dispersed Pt (in red circle) on Ru nanoclusters in $Pt_{0.47}$-Ru/Acet catalyst can be observed due to the higher weight of Pt element than Ru. Hence, the intensity of atomic Pt is larger than surrounding Ru atoms (Figure 1d). In addition, the well-defined lattice spacing of 0.234 nm belongs to the (100) plane of Ru (Figure 1d). And EDS mapping further presents that Ru and Pt elements are evenly distributed throughout the structure (Figure 1e).

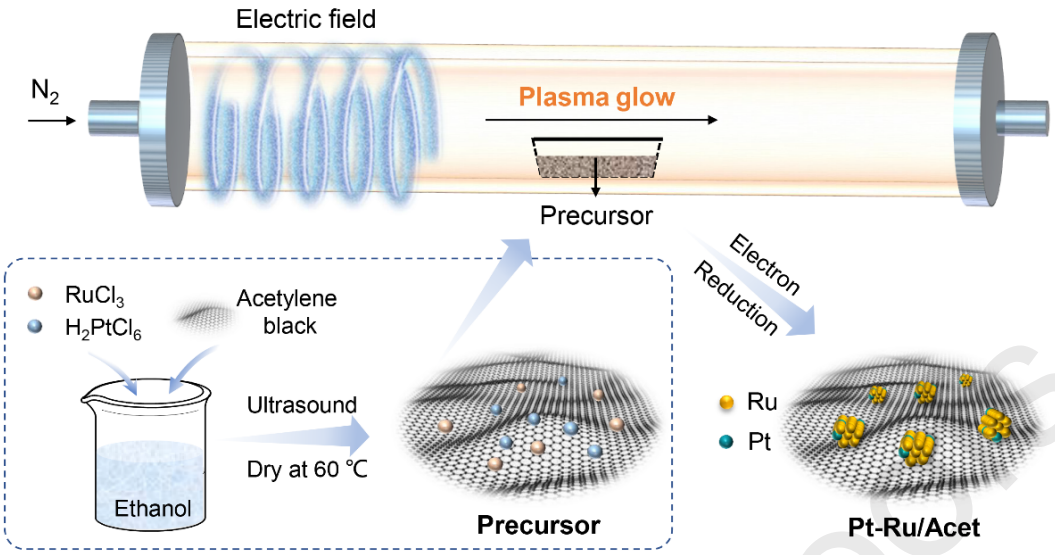

Scheme 1. Schematic illustration of the synthesis of $Pt_{0.47}$-Ru/Acet.

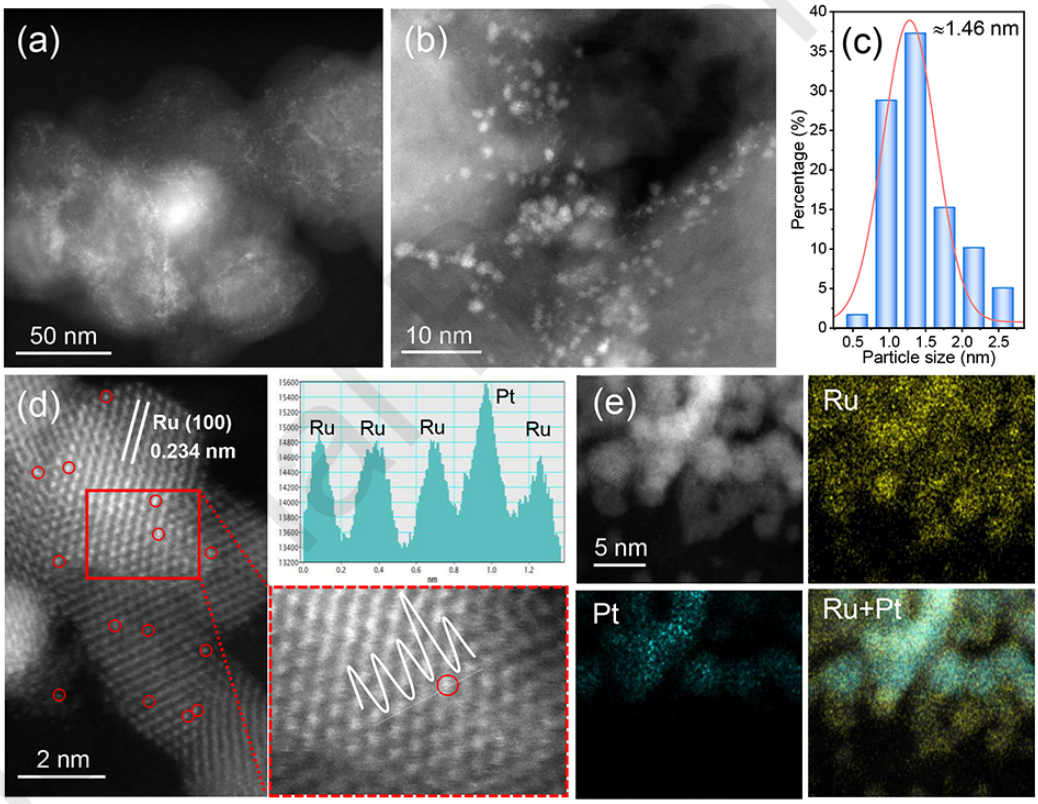

Figure 1. **The structural characterization on $Pt_{0.47}$-Ru/Acet.** (a, b) The STEM images of $Pt_{0.47}$-Ru/Acet. (c) the corresponding nanoparticle size distribution of $Pt_{0.47}$-Ru/Acet. (d) Atomic-resolution HAADF-STEM image. Magnified image in the red box, Pt atom was marked with red circles. (e) EDS elemental maps of Ru and Pt.

The XPS was performed to analyze the electronic structure and chemical states of the $Pt_{0.47}$-Ru/Acet catalyst. As seen from the high-resolution Ru 3p XPS spectra of the as-prepared catalysts displayed in Figure 2a and Figure S7a, the binding energy peaks of all catalysts at 462.56 eV and 484.58 eV belong to Ru $3p_{3/2}$ and Ru $3p_{1/2}$ of metallic Ru, respectively. The deconvoluted peaks at 466.94 eV and 487.67 eV are separately attributed to Ru $3p_{3/2}$ and Ru $3p_{1/2}$ of Ru^{n+} [45]. According to the proportion (6:1) of metal Ru/Ru^{n+} in the catalyst, it is known that the Ru element mainly exists in a metallic state. In the Pt 4f spectra (Figure 2b), the binding energy peaks of $Pt_{0.47}$-Ru/Acet at 73.26 eV and 76.57 eV are attributed to Pt $4f_{7/2}$ and Pt $4f_{5/2}$ of Pt^{2+}, respectively [42, 46]. Compared to $Pt_{0.47}$/Acet, Pt 4f binding energies of $Pt_{0.47}$-Ru/Acet are negatively shifted by 0.21 eV. Meanwhile, in Figure S7b, the absorption peaks of Pt 4f with the increase of Pt content shift toward lower binding energy, and the peaks of Pt^0 can be observed in Pt 4f spectra for $Pt_{2.04}$-Ru/Acet, further indicating that electrons are transferred to Pt surface, which is identical with the DFT results. Based on the XPS analysis, the chemical states of Ru and Pt elements in the $Pt_{2.04}$-Ru/Acet catalyst are 0 and +2, respectively, which indicate that the Ru^{3+} and Pt^{4+} in the precursor can be successfully reduced in the process of plasma treatment.

X-ray absorption fine structure was conducted to further investigate the electronic structure and coordination environment of Ru and Pt in $Pt_{0.47}$-Ru/Acet catalyst. Figure 2c displays the X-ray absorption near-edge structure (XANES) of Ru K-edge for $Pt_{0.47}$-Ru/Acet, with the K-edge spectrum of Ru foil and RuO_2 as references, it can be seen that the absorption edge of $Pt_{0.47}$-Ru/Acet almost coincides with the Ru foil, manifesting that the valence state of Ru for $Pt_{0.47}$-Ru/Acet mainly exists in a metallic state, which is consistent with the XPS analysis result. The XANES spectra of Pt L_3-edge in Pt foil, PtO_2, and $Pt_{0.47}$-Ru/Acet are shown in Figure 2d, and the white line intensity of Pt L_3-edge corresponds to the transition from occupied Pt $2p_{3/2}$ electron to empty $5d_{5/2}$ orbital, which is indicative of 5d-band occupancy [47, 48]. The more 5d vacant orbital, the greater electron transition probability, which reflects the higher intensity of the white line. Namely, the higher intensity the white line indicates the higher oxidation state of Pt. Notably, the

intensity of the white line for $Pt_{0.47}$-Ru/Acet is between Pt foil and PtO_2, indicating that the average valence state of Pt is between 0 and +4. Combined with the XPS analysis and the fitted average oxidation states of Pt for $Pt_{0.47}$-Ru/Acet from XANES spectra (Table S2), it can be known that Pt is mainly in the form of Pt^{2+}. Moreover, in Figure 2e, the Ru K-edge extended X-ray absorption fine structure (EXAFS) spectrum of $Pt_{0.47}$-Ru/Acet exhibits a primary peak at 2.38Å, which belongs to the Ru–Ru bond (Figure S8a). Notably, the Ru–Ru coordination peak of $Pt_{0.47}$-Ru/Acet is higher than the distance of the nearest coordination shells of Ru atoms in the Ru foil, indicating that there is an interaction between Ru and Pt atoms. According to the Pt L_3-edge EXAFS spectra shown in Figure 2f, there is no obvious peak at 2.42 Å (for Pt–Pt coordination in metallic Pt), but the peak around 2.51 Å could be ascribed to the Pt-Ru bond, which is further demonstrated by EXAFS curve fitting analysis (Figure S8b). And the EXAFS spectra imply that most Pt species are distributed on Ru nanoclusters in the form of isolated atoms.

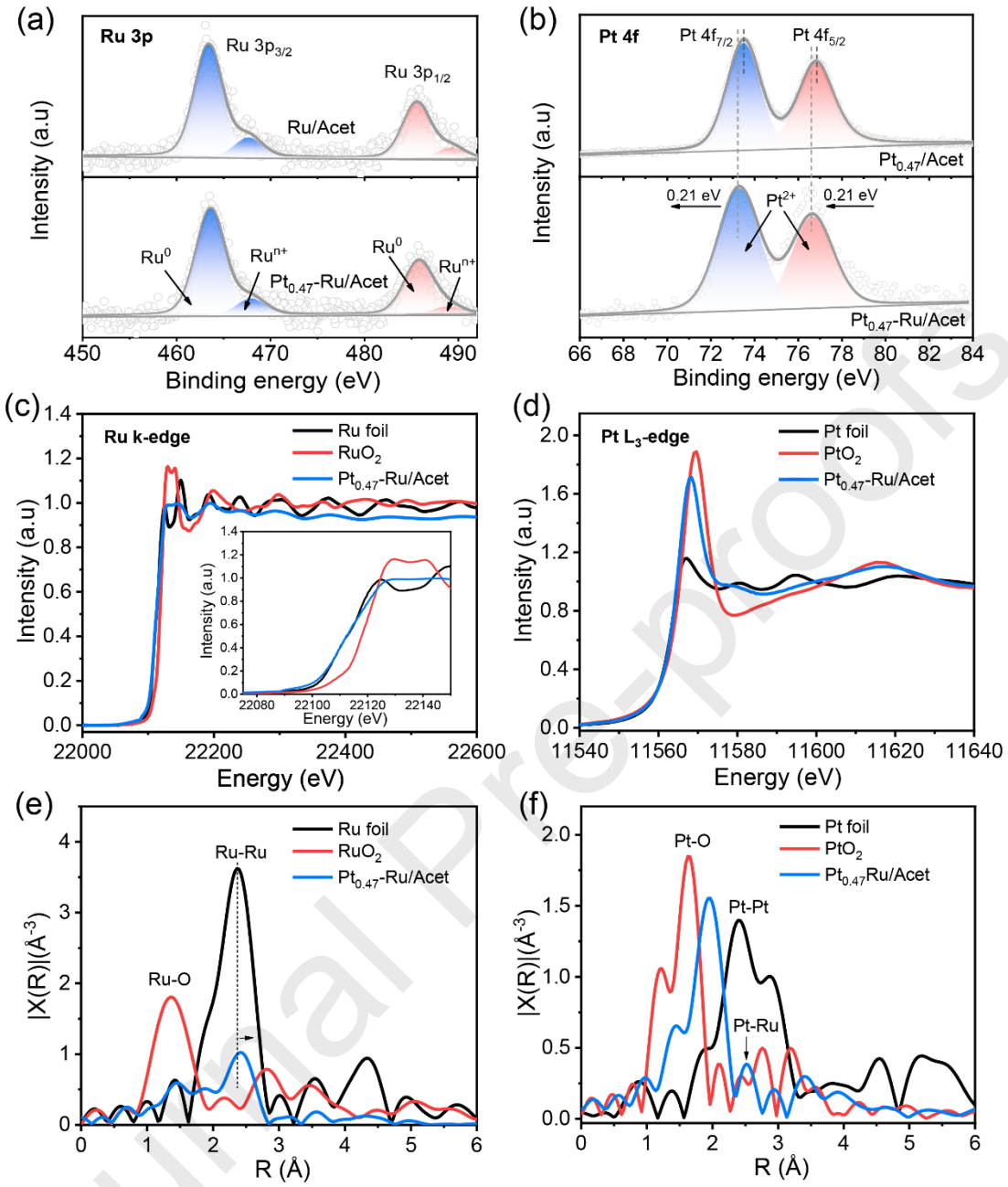

Figure 2. High-resolution XPS spectra of the as-prepared samples for (a) Ru 3p and (b) Pt 4f, (c) Ru K-edge XANES spectra of Ru foil, RuO_2, and $Pt_{0.47}$-Ru/Acet. (d) Pt L_3-edge XANES spectra of Pt foil, PtO_2, and $Pt_{0.47}$-Ru/Acet. (e) Fourier transforms of EXAFS spectra of Ru foil, RuO_2, and $Pt_{0.47}$-Ru/Acet. (f) Fourier transforms of EXAFS spectra of Pt foil, PtO_2, and $Pt_{0.47}$-Ru/Acet.

3.2 Electrocatalytic performance of catalysts

To elucidate the advantage of plasma treatment, we compared the HER activities

of Ru/Acet catalyst prepared by low-temperature plasma technology and Ru/Acet-Calc catalyst obtained by calcination method. It can be seen from Figure S9 that Ru/Acet displays a lower overpotential (η_{10} = 42 mV) than that of Ru/Acet-Calc catalyst (η_{10} = 82 mV), and the electrochemical active surface areas (ECSA) value of Ru/Acet is also higher (in Figure S10 and Table S7). Combined with TEM analysis, this electrocatalytic performance improvement should be ascribed to the decrease in agglomeration of nanoclusters and then exposure to more active sites. Compared with Ru/Acet catalyst, the HER activities of pure Ni foam (η_{10} = 261 mV) and Acet (η_{10} = 193 mV) can be almost negligible (Figure 3a), indicating that Ru nanoclusters are the main active component in the catalyst. To further improve the alkaline HER performance of Ru/Acet, atomically dispersed Pt was introduced on the Ru nanoclusters surface ($Pt_{0.47}$-Ru/Acet). As shown in Figure 3a, The $Pt_{0.47}$-Ru/Acet with 0.47 wt% doping amount of Pt single atoms exhibits high HER activity with low overpotentials of 17 mV (η_{10}) and 115 mV (η_{100}) in 1 M KOH solution, respectively, which are obviously superior to commercial Ru/C (η_{10} = 43 mV, η_{100} = 169 mV) and 20 wt% Pt/C (η_{10} = 23 mV, η_{100} = 143 mV) (Figure 3b). Meanwhile, the overpotential (η_{10}) of $Pt_{0.47}$-Ru/Acet is reduced by 25 mV and 163 mV compared with Ru/Acet (η_{10} = 42 mV) and $Pt_{0.47}$/Acet (η_{10} = 180 mV), respectively. And this significantly enhanced HER activity demonstrates the cooperative effects between Ru nanoclusters and Pt single atoms. And the overpotentials of these catalysts at current densities of 10 $mA \cdot cm^{-2}$ and 100 $mA \cdot cm^{-2}$ are shown in Figure 3c. Moreover, the influence of Pt content on the HER activity of Pt-Ru/Acet was investigated, as shown in Figure S11, after introducing a small amount of Pt into the Ru/Acet, these Pt-Ru/Acet catalysts exhibit enhanced HER performance. Even the doping amount of Pt single atoms is only 0.11 wt%, the performance of the catalyst is significantly improved and the overpotential (η_{10}) is as low as 23 mV. Nevertheless, when the Pt content continues to increase from 0.47 wt% to 2.04 wt%, the overpotential (η_{10}) of the $Pt_{2.04}$-Ru/Acet catalyst only decreases by 6 mV, indicating the HER performance does not increase significantly with Pt content. This may be attributed to the larger particle size of Pt-Ru/Acet when the Pt content is excessive, resulting in decreased exposure of some

effective active sites. Meanwhile, the mass activity of $Pt_{2.04}$-Ru/Acet catalyst (1.22 $A \cdot mg_{metal}^{-1}$) is lower than that of $Pt_{0.47}$-Ru/Acet (1.33 $A \cdot mg_{metal}^{-1}$) at an overpotential of 100 mV. Thus, based on the cost and HER performance into account, the $Pt_{0.47}$-Ru/Acet catalyst is used in subsequent experiments. Additionally, the remarkable HER performance of $Pt_{0.47}$-Ru/Acet is also better than the most previously reported electrocatalysts (Figure 3g and Table S5).

The Tafel slope of $Pt_{0.47}$-Ru/Acet in Figure 3d is 66 $mV \cdot dec^{-1}$, lower than that of Ru/Acet (73 $mV \cdot dec^{-1}$) and $Pt_{0.47}$/Acet (168.7 $mV \cdot dec^{-1}$), which reflects the faster reaction kinetics and suggests a Volmer-Heyrovsky mechanism for $Pt_{0.47}$-Ru/Acet [16, 49]. Furthermore, the fitted electrochemical impedance spectrogram (EIS) and the corresponding charge transfer resistance (R_{ct}) are obtained according to the equivalent circuit fitting diagram (Figure 3e). Generally speaking, the smaller radius of the arc for the impedance spectrum, the lower value of charge transfer resistance, implying a faster reaction rate. Apparently, the $Pt_{0.47}$-Ru/Acet presents smaller R_{ct} values (Table S6) than Ru/Acet and $Pt_{0.47}$/Acet, indicating more efficient charge transfer at the interface of $Pt_{0.47}$-Ru/Acet and electrolyte.

Electrochemical active surface areas (ECSA) of catalysts were evaluated via the double-layer capacitance (C_{dl}) measurements obtained by way of cyclic voltammetry versus scan rates (Figure S12) [50]. The large value of C_{dl} gives a high ECSA for $Pt_{0.47}$-Ru/Acet, nearly comparable to that of Ru/Acet (Figure 3f and Table S7), highlighting that Pt in the form of single atoms modified the Ru nanoclusters avoids the blocking of surface electrochemically reactive sites by the modifier to the maximum extent, maintaining a higher ECSA. Furthermore, the mass activity plays a crucial role in the economic effect of catalysis, determining the cost of catalyst [14, 51]. Figure S13 presents the mass activities of Ru/Acet, $Pt_{0.47}$-Ru/Acet, commercial Ru/C, and 20 wt% Pt/C at overpotentials of 50 and 100 mV. The $Pt_{0.47}$-Ru/Acet displays higher mass activities than Ru/Acet and commercial 20 wt% Pt/C, notably, $Pt_{0.47}$-Ru/Acet with a mass activity of 0.51 $A \cdot mg_{Ru}^{-1}$ at 50 mV is about 4.05, 1.96 and 1.64 times that of commercial Ru/C (0.126 $A \cdot mg_{Ru}^{-1}$), 20 wt% Pt/C (0.26 $A \cdot mg_{Pt}^{-1}$) and Ru/Acet (0.31 $A \cdot mg_{Ru}^{-1}$), respectively, outperforming reported Ru-based catalysts

such as Ru-3DNCN (0.13 $A \cdot mg_{Ru}^{-1}$) [29], Ru-C-H_2O-CH_3CH_2OH (0.29 $A \cdot mg_{Ru}^{-1}$) [52], Ru NCs-BNG (0.5 $A \cdot mg_{Ru}^{-1}$) [28], $NiRu_{0.13}$-BDC (0.125 $A \cdot mg_{Ru}^{-1}$) [33], Ru-MoO_2 (0.38 $A \cdot mg_{Ru}^{-1}$) [53], and RuNi-NCNFs (0.16 $A \cdot mg_{Ru}^{-1}$) [54]. Turnover frequency (TOF) is used to quantify the intrinsic activity of the catalyst [14, 55]. The TOF value for $Pt_{0.47}$-Ru/Acet at an overpotential of 100 mV is calculated to be 0.7 $H_2 \cdot s^{-1}$, which surpasses that of commercial 20 wt% Pt/C (0.22 $H_2 \cdot s^{-1}$).

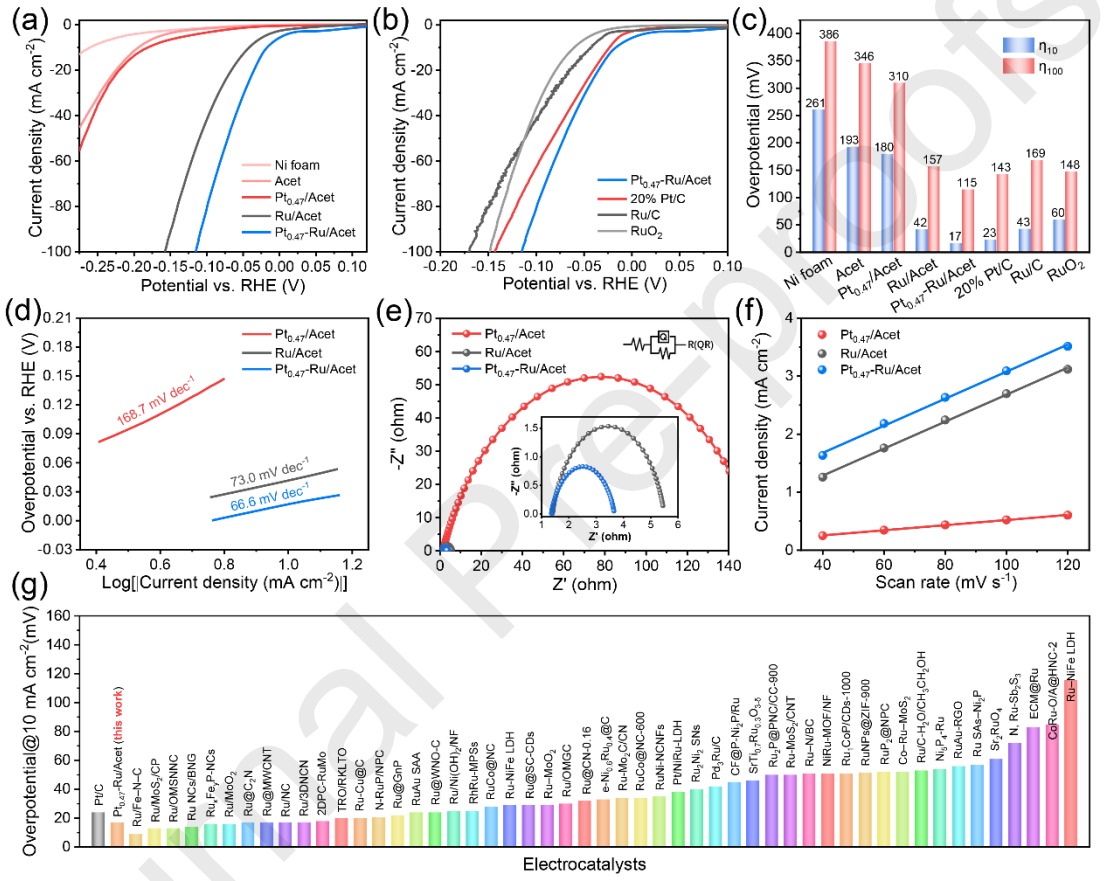

Figure 3. HER performance of the as-prepared catalysts in 1 M KOH solution. (a) and (b) LSV polarization curves (iR corrected) of Ni foam, Acet, Ru/Acet, $Pt_{0.47}$-Ru /Acet, commercial 20 wt% Pt/C, 5 wt% Ru/C, and RuO_2 at a scan rate of 10 mV s^{-1}. (c) Corresponding overpotentials at 10 mA cm^{-2} and 100 mA cm^{-2}. (d) Tafel slopes from the polarization curves. (e) EIS spectra of different electrocatalysts. (f) Corresponding electrochemical double layer capacitances. (g) Comparison of the HER activity for Ru-based electrocatalysts with other reported in 1 M KOH solution.

The promotion effect of Pt modification is also revealed by CV curves in Figure

4a. All the CVs of Pt-Ru catalyst present three regions as follows [56]: region I, the cathode peaks of hydrogen underpotential deposition (H_{upd}) adsorption region (0-0.25 V), region II, hydrogen evolution region (<0 V), and region III, the anodic peaks of absorbed hydrogen desorption region (0-0.25 V). It has been reported that the hydrogen binding energy (HBE) of a catalyst can be evaluated by comparing the peak potential of absorbed hydrogen desorption, and the larger area of absorbed hydrogen desorption peak indicates that more absorbed hydrogen would be generated on the catalyst surface [57, 58]. Compared with Ru/Acet and $Pt_{2.04}$/Acet, the peak potential of hydrogen desorption for Pt-Ru/Acet gradually decreases with the increase of Pt content, which implies that the Pt-Ru nanoclusters have lower HBE due to the weaker Ru-H bond after the introduction of Pt, benefiting to the desorption of adsorbed hydrogen on the catalyst surface. Furthermore, the Pt-Ru/Acet exhibits obvious larger areas of adsorbed hydrogen desorption peak (region III) and current density (at η_{100}) than Ru/Acet and Pt/Acet (Figure 4b), implying that more absorbed hydrogen can be produced on the Pt-Ru/Acet surface during the HER process, which would accelerate the evolution of H_2.

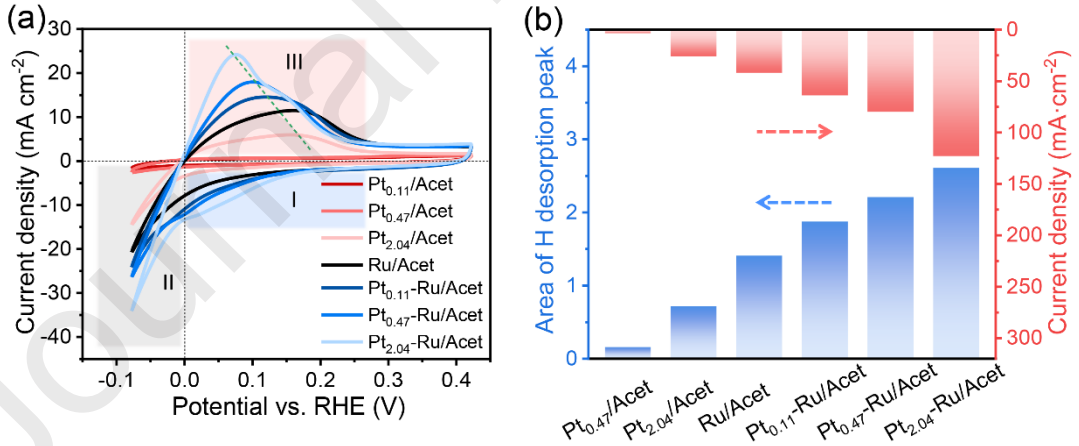

Figure 4. (a) The stabilized CV curves for $Pt_{0.11}$/Acet, $Pt_{0.47}$/Acet, Ru/Acet, $Pt_{2.04}$/Acet, $Pt_{0.11}$-Ru/Acet, $Pt_{0.47}$-Ru/Acet, and $Pt_{2.04}$-Ru/Acet catalysts in 1 M KOH solution. (b) Corresponding the area of H desorption peak and current density at η_{100}.

The HER performance of $Pt_{0.47}$-Ru/Acet catalyst was further investigated in acidic and neutral electrolytes. As shown in Figure 5a, the $Pt_{0.47}$-Ru/Acet catalyst presents an overpotential of 28 mV at a current density of 10 mA·cm^{-2} in 0.5 M H_2SO_4, which is

significantly lower than that of Ru/Acet (141 mV) and $Pt_{0.47}$/Acet (72 mV), implying a cooperative effect between Ru nanoclusters and Pt single atoms. Meanwhile, the $Pt_{0.47}$-Ru/Acet catalyst reaches the lower overpotential of 8 mV at a current density of 10 $mA \cdot cm^{-2}$ in 1 M PBS electrolyte. Furthermore, the $Pt_{0.47}$-Ru/Acet catalyst displays the lager mass activity values of 2.63 and 0.85 $A \cdot mg^{-1}$ at overpotential of 100 mV in acidic and neutral media, respectively, exceeding to commercial Ru/C (0.05 $A \cdot mg^{-1}$, 0.09 $A \cdot mg^{-1}$) and 20 wt% Pt/C (2.08 $A \cdot mg^{-1}$, 0.17 $A \cdot mg^{-1}$) (Figure 5b and d). The Tafel slope of $Pt_{0.47}$-Ru/Acet is 33.3 and 94.4 $mV \cdot dec^{-1}$ in 0.5 M H_2SO_4 and 1 M PBS electrolyte, respectively, suggesting the faster reaction kinetics (Figure 5c and e,). Furthermore, the HER activities evaluated by overpotential at 10 $mA \cdot cm^{-2}$ of $Pt_{0.47}$-Ru/Acet compared with the reported Ru-based catalysts in acidic and neutral media are summarized (Figure 5g and h, Table S8 and S9), indicating that $Pt_{0.47}$-Ru/Acet possess an excellent catalytic activity to HER at all pH values. In addition, the oxygen evolution reaction (OER) activity of $Pt_{0.47}$-Ru/Acet was also studied in 1 M KOH solution (Figure S14a). The overpotentials of $Pt_{0.47}$-Ru/Acet are 307 mV at 10 $mA \cdot cm^{-2}$, which is much lower than that of Ru/Acet (340 mV) and $Pt_{0.47}$/Acet (390 mV), suggesting a good OER performance of $Pt_{0.47}$-Ru/Acet under alkaline conditions. Furthermore, the $Pt_{0.47}$-Ru/Acet presents a smaller radiu of the arc for the impedance spectrum than Ru/Acet and $Pt_{0.47}$/Acet (Figure S14b), indicating more efficient charge transfer.

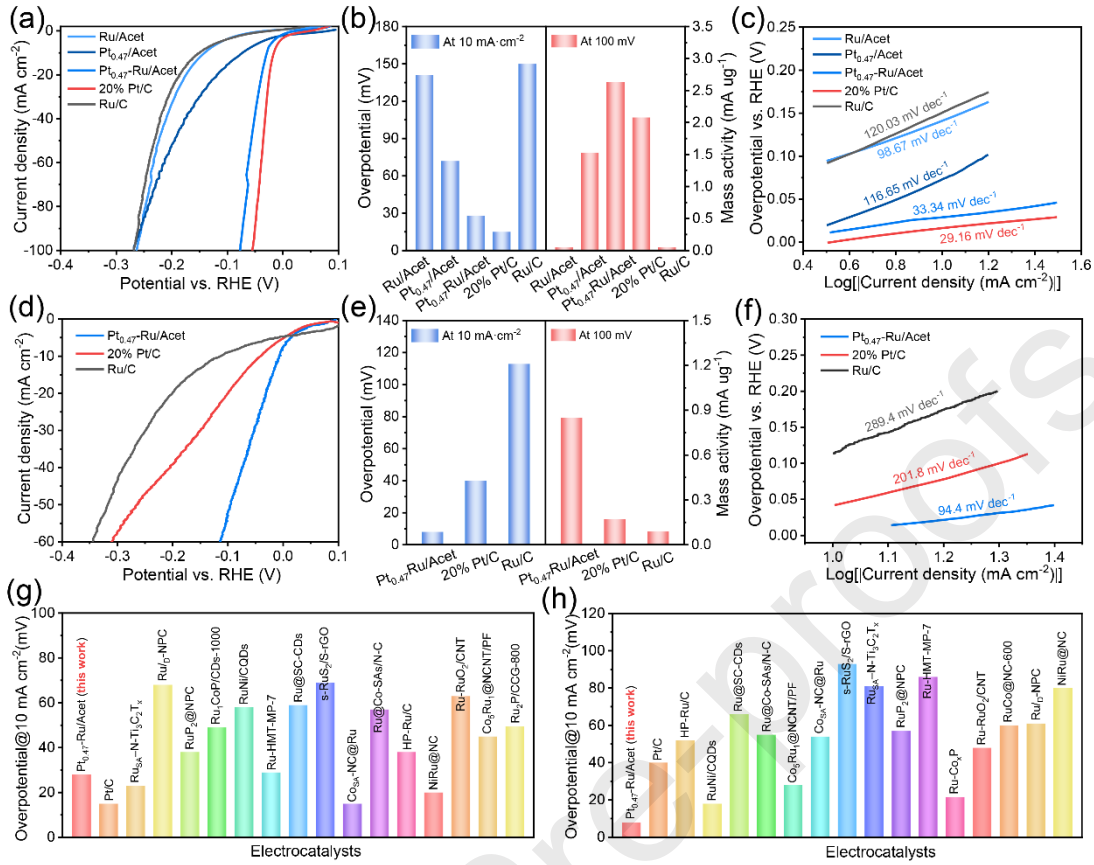

Figure 5. HER performance of the as-prepared catalysts in 0.5 M H_2SO_4 and 1M PBS solution. LSV polarization curves (iR corrected) of $Pt_{0.47}$-Ru/Acet, commercial 20 wt% Pt/C, and 5 wt% Ru/C in 0.5 M H_2SO_4 (a) and 1 M PBS (d). Corresponding overpotentials and mass activity in 0.5 M H_2SO_4 (b) and 1 M PBS (e). Tafel slopes from the polarization curves (c) and (f). Comparison of the HER activity for Ru-based electrocatalysts with others reported in 0.5 M H_2SO_4 (g) and 1 M PBS (h).

3.3 DFT calculations

Density functional theory (DFT) calculations expounded the underlying mechanism responsible for the excellent alkaline HER activity of Pt-Ru/Acet catalyst. Pt-Ru (001), (100), (101) facets commonly adopted for theoretical studies [49, 59, 60] were modeled, respectively, and for comparison, Ru (001), (100), (101) and Pt (111) facets were also simulated. Generally, there are two key processes involved in alkaline HER, including the breaking of the H-O bond in H_2O to form H* intermediates (Volmer step: $H_2O + e^- \rightarrow H^* + OH^-$) and subsequent recombination of

produced H* into H_2 (Heyrovsky step: $H_2O + e^- + H^* \rightarrow H_2 + OH^-$ or Tafel step: $H^* + H^* \rightarrow H_2$) [3, 13]. The adsorption and dissociation of water are first investigated. As shown in Figure S15, the adsorption energies of Pt-Ru (001), (100), and (101) surface for H_2O molecule are -0.72, -0.78, and -0.70 eV, respectively, which are close to that of Ru (001), (100) and (101) surface, but obviously higher than that of Pt (111) surface (-0.46 eV), indicating that H_2O molecule tends to be adsorbed on Ru sites. Moreover, as displayed in Figure 6a, the energy barrier of the transition state (TS) for water dissociation on the Pt-Ru (100) surface is 0.79 eV, which is lower than that of the Ru (100) surface and Pt (111) surface, and the similar conclusion can be observed on the Pt-Ru (001) surface and Pt-Ru (101) surface (Figure S16). The lower energy barrier of water dissociation on the Pt-Ru surface implies that the H_2O molecule is easier to be dissociated into OH* and H* on the Pt-Ru surface, and the water dissociation kinetic is obviously facilitated by Pt single atoms modification, which could accelerate the formation rate of H*. Next, the Heyrovsky step is calculated because the alkaline HER process on the Pt-Ru/Acet catalyst follows the Volmer-Heyrovsky pathway confirmed by the experimental result (Tafel slope). Pt-Ru (100) presents a significantly lower energy barrier of Heyrovsky step (0.45 eV) compared with Ru (100) surface (1.05 eV) and Pt (111) surface (1.45 eV) as shown in Figure 6b, meanwhile, the analogous regulation can be observed on the Pt-Ru (001) surface and Pt-Ru (101) surface (Figure S17). And the calculated energy diagrams for the Vomer step (ΔG_1) and Heyrovsky step (ΔG_2) on the Pt-Ru, Ru, and Pt over various surfaces (001), (101), (100), and (111) are shown in Figure 6c. The low energy barriers of the Volmer step and Heyrovsky step on the Pt-Ru surface support the excellent alkaline HER activity. Furthermore, the charge density distributions on the Pt-Ru (001), (101), and (100) were simulated to investigate the electronic structure of the Pt-Ru/Acet catalyst. As shown in Figure 6d, there is an obvious charge depletion around Ru while distinct charge accumulation around Pt single atoms, with a certain number of electrons (0.42 eV) transferred from Ru to Pt atom, indicating the charge interaction between Pt single atoms and Ru, which is consistent with the XPS results. Based on DFT calculated results, the alkaline HER process on Pt-Ru/Acet can be illustrated in

Figure 6e. Specifically, H_2O molecules are firstly absorbed on the Ru site in the basic electrolyte and then dissociated into intermediate OH* and H* via the Volmer step. Subsequently, the produced H* could react with another H_2O molecule to form H_2 (Heyrovsky step). The DFT calculations reveal that the electronic structure of Ru would be affected by introducing atomically dispersed Pt on the Ru nanoclusters surface, and the energy barriers of water dissociation (Volmer step) and subsequent hydrogen evolution (Heyrovsky step) are reduced, thus leading to improved HER performance in the alkaline.

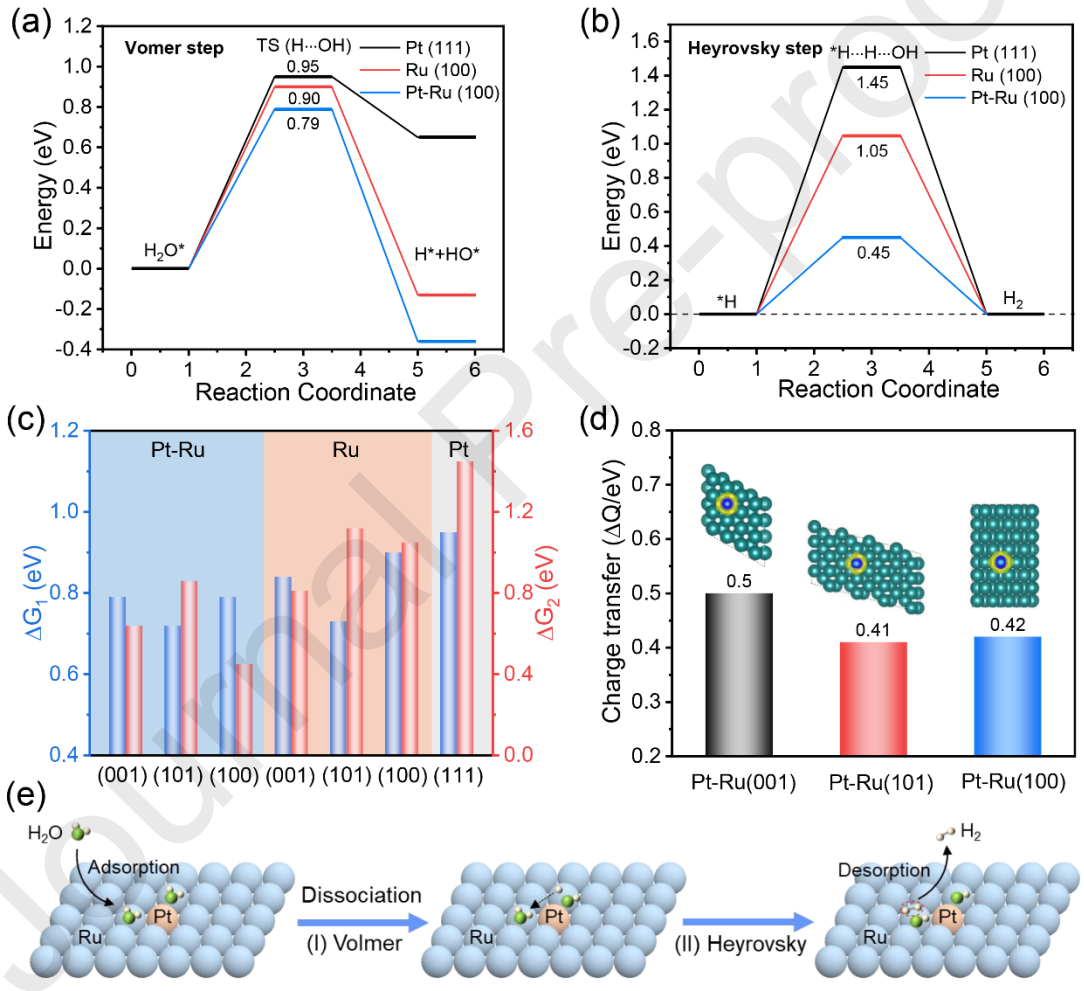

Figure 6. DFT calculations. Energy diagrams of water dissociation (a) and Heyrovsky step (b) for Pt-Ru (001), Ru (100), and Pt (111), respectively. (c) The calculated energy diagrams for the Volmer step (ΔG_1) and Heyrovsky step (ΔG_2) on the Pt-Ru, Ru, and Pt over various exposed surfaces (001), (101), (100), and (111). (d) The value of charge transfer from Ru to Pt on Pt-Ru (001), Pt-Ru (101), and Pt-Ru

(100) surface.

3.4 Stability and overall water splitting

The electrocatalytic stability of $Pt_{0.47}$-Ru/Acet was investigated via time-dependent current density curves (i~t) and CV cycling. As depicted in Figure 7a, after 30 h of continuous testing in 1 M KOH electrolyte, the loss of current density at 20 $mA \cdot cm^{-2}$ is about 25%, and the overpotential (η_{10}) of $Pt_{0.47}$-Ru/Acet increases from 17 mV to 55 mV seeing from the LSV polarization curves in Figure S18a, implying the attenuation of HER activity. However, this LSV curve after CV scanning in the range of -0.5 to -1 V (Figure S18b) almost coincides with the original LSV curve (Figure S18c), suggesting that the HER activity of $Pt_{0.47}$-Ru/Acet can be regenerated by CV activation and there is barely loss of active components in the catalyst during the chronopotentiometry test. Generally, the deactivation of the electrocatalyst is mainly caused by the following two aspects: (1) the loss of active components in the catalyst; (2) the poisoning of intermediate species. Figure S18d presents the CV curves of $Pt_{0.47}$-Ru/Acet before and after 30 h of i~t tests, it can be seen that the area of hydrogen desorption peak for $Pt_{0.47}$-Ru/Acet after 30 h of i~t test is larger, indicating that the more intermediate species are generated and cover the active sites on the catalyst surface during i~t tests, and these intermediate species can be removed after CV redox activation. Thus the active sites are exposed again, and the HER performance of catalyst is restored [56]. Furthermore, the stability of $Pt_{0.47}$-Ru/Acet was studied by CV (Figure 7b). After 8000 CV cycles, there is barely performance decrease for $Pt_{0.47}$-Ru/Acet, displaying a stable HER activity. Based on the above analysis, it is shown that the $Pt_{0.47}$-Ru/Acet catalyst presents a good stability and reproducibility.

Inspired by the excellent alkaline HER performance of $Pt_{0.47}$-Ru/Acet catalyst, we further assemble a two-electrode asymmetric electrolyzer by using $Pt_{0.47}$-Ru/Acet catalyst (as a cathode) coupled with RuO_2 (as an anode) in 1 M KOH to investigate the overall water splitting (Figure 7c). As shown in the polarization curves of Figure 7d, the $Pt_{0.47}$-Ru/Acet || RuO_2 electrolyzer has a good activity for overall water

splitting with a cell voltage of 1.543 V at 10 mA · cm^{-2} in 1 M KOH, which is equivalent to that of the commercial Pt/C || RuO_2 electrolyzer (1.539 V). Meanwhile, the chronopotentiometry curve (Figure 7d, inset) displays a negligible potential change after a continuous 12 h operation, which indicates that $Pt_{0.47}$-Ru/Acet || RuO_2 electrolyzer could stably run in a long-term electrochemical overall water splitting test. In addition, $Pt_{0.47}$-Ru/Acet || $Pt_{0.47}$-Ru/Acet electrolyzer also displays fine water splitting performance (1.588 V at 10 mA · cm^{-2}) due to the good OER activity of $Pt_{0.47}$-Ru/Acet, especially the required voltage under high current is obviously lower than that of commercial Pt/C || RuO_2 electrolyzer. Furthermore, the construction of a solar-hydrogen system is a promising approach to achieving economical and sustainable hydrogen production in practical applications. Herein, a commercial solar panel is used to drive the overall water splitting (1.553 V) of $Pt_{0.47}$-Ru/Acet || RuO_2 electrolyzer under sunlight illumination (Figure 7e, magnified image). It can be seen that H_2 and O_2 bubbles are continuously generated from the two electrode surfaces, respectively (Figure 7e and video S1), implying it has the potential to convert low-voltage electric energy produced by sunlight into chemical energy.

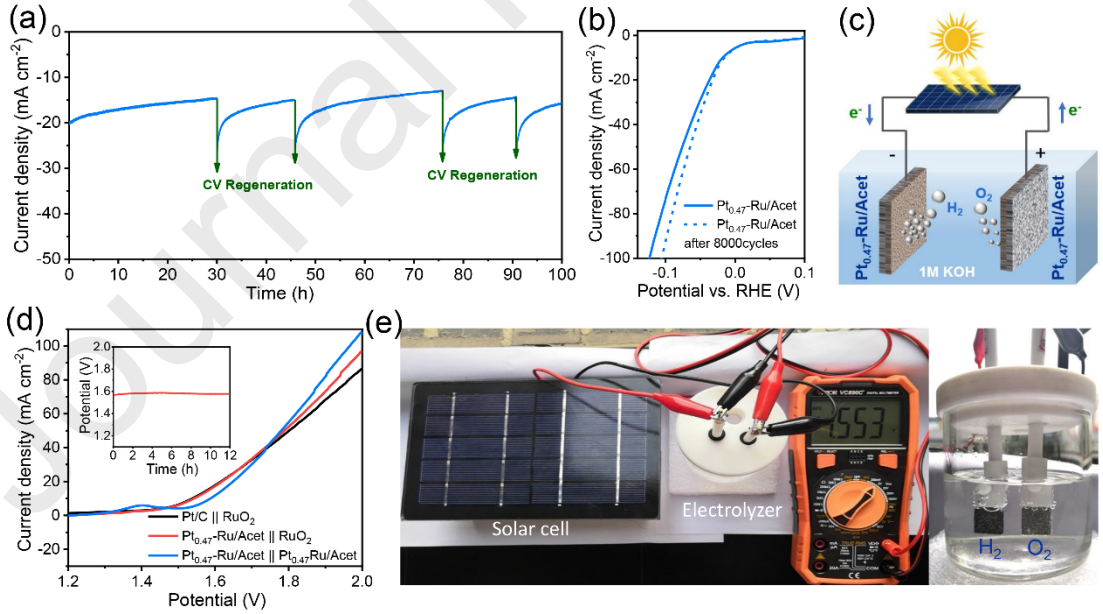

Figure 7. Stability and overall water splitting. (a) i-t curves of $Pt_{0.47}$-Ru/Acet at an overpotential of 20 mA cm^{-2}. (b) LSV curves of $Pt_{0.47}$-Ru/Acet before and after 8000 CV cycles with graphite rod as the counter electrode. (c) Schematic diagram of the photovoltaic-driven overall water splitting. (d) LSV polarization curves of $Pt_{0.47}$-

Ru/Acet || $Pt_{0.47}$-Ru/Acet, $Pt_{0.47}$-Ru/Acet || RuO_2, Pt/C || RuO_2 electrolyzer for overall water splitting in 1M KOH without iR compensation. Inset: chronopotentiometry curve of $Pt_{0.47}$-Ru/Acet || RuO_2 for 12h. (e) photograph of the integrated water splitting device with solar panel assisted and the magnified image of the electrolyzer.

4. Conclusions

In summary, Pt single atoms modified Ru nanoclusters supported on the commercial acetylene black have been successfully fabricated by a facile cold-plasma technique. Compared to a significantly larger size (7.32 nm) of Ru nanoparticles obtained by the calcination method, Ru nanoclusters (~1.41 nm) highly dispersed on the acetylene black (Ru/Acet) can be prepared by low-temperature plasma technology, which would expose more active sites. The as-prepared atomically dispersed Pt on ultrafine Ru nanoclusters catalyst ($Pt_{0.47}$-Ru/Acet) displays excellent HER activity with low overpotentials of 17 mV and 115 mV to achieve a current density of 10 mA·cm^2 and 100 mA·cm^2 in 1 M KOH, respectively. Notably, the mass activity of $Pt_{0.47}$-Ru/Acet at an overpotential of 100 mV is about 5.54 and 2.15 times that of commercial Ru/C and Pt/C catalysts at an overpotential of 100 mV, respectively. Meanwhile, the $Pt_{0.47}$-Ru/Acet catalyst shows a low overpotential of 28, and 8 mV at 10 mA·cm^{-2} in 0.5 M H_2SO_4, and 1 M PBS, respectively. The $Pt_{0.47}$-Ru/Acet catalyst also has good stability and the HER activity after a period of the i~t test can be completely regenerated by CV activation. DFT calculations reveal that the electronic structure of Ru would be regulated by introducing atomically dispersed Pt on the Ru nanoclusters surface, and the energy barriers of water dissociation (Volmer step) and subsequent hydrogen evolution (Heyrovsky step) are reduced, thus leading to improved HER performance in the alkaline. In addition, $Pt_{0.47}$-Ru/Acet catalyst also displays bifunctionality in both HER and OER and thus can be well adapted in assembled two-electrode overall water splitting system.

References

[1] N. Mahmood, Y. Yao, J.W. Zhang, L. Pan, X. Zhang, J.J. Zou, Electrocatalysts for

Hydrogen Evolution in Alkaline Electrolytes: Mechanisms, Challenges, and Prospective Solutions, Adv. Sci. 5 (2018) 1700464.

[2] Z.Y. Yu, Y. Duan, X.Y. Feng, X. Yu, M.R. Gao, S.H. Yu, Clean and Affordable Hydrogen Fuel from Alkaline Water Splitting: Past, Recent Progress, and Future Prospects, Adv. Mater. 33 (2021) 2007100.

[3] X. Wang, Y. Zheng, W. Sheng, Z.J. Xu, M. Jaroniec, S.-Z. Qiao, Strategies for design of electrocatalysts for hydrogen evolution under alkaline conditions, Mater. Today. 36 (2020) 125-138.

[4] C. Hu, L. Zhang, J. Gong, Recent progress made in the mechanism comprehension and design of electrocatalysts for alkaline water splitting, Energy Environ. Sci. 12 (2019) 2620-2645.

[5] J.K. Norskov, C.H. Christensen, Toward Efficient Hydrogen Production at Surfaces, Science 312 (2006) 1322-1323.

[6] Z. Wang, S. Shen, Z. Lin, W. Tao, Q. Zhang, F. Meng, L. Gu, W. Zhong, Regulating the Local Spin State and Band Structure in Ni_3S_2 Nanosheet for Improved Oxygen Evolution Activity, Adv. Funct. Mater. 32 (2022) 2112832.

[7] M.R. Shaner, H.A. Atwater, N.S. Lewis, E.W. McFarland, A comparative technoeconomic analysis of renewable hydrogen production using solar energy, Energy Environ. Sci. 9 (2016) 2354-2371.

[8] S. Shen, Z. Wang, Z. Lin, K. Song, Q. Zhang, F. Meng, L. Gu, W. Zhong, Crystalline-Amorphous Interfaces Coupling of $CoSe_2$ /CoP with Optimized d-Band Center and Boosted Electrocatalytic Hydrogen Evolution, Adv. Mater. 34 (2022) 2110631.

[9] Y. Zheng, Y. Jiao, Y. Zhu, L.H. Li, Y. Han, Y. Chen, M. Jaroniec, S.Z. Qiao, High Electrocatalytic Hydrogen Evolution Activity of an Anomalous Ruthenium Catalyst, J. Am. Chem. Soc. 138 (2016) 16174-16181.

[10] D. Liu, X. Li, S. Chen, H. Yan, C. Wang, C. Wu, Y.A. Haleem, S. Duan, J. Lu, B. Ge, P.M. Ajayan, Y. Luo, J. Jiang, L. Song, Atomically dispersed platinum supported on curved carbon supports for efficient electrocatalytic hydrogen evolution, Nat. Energy 4 (2019) 512-518.

[11] Y. Zheng, Y. Jiao, A. Vasileff, S.Z. Qiao, The Hydrogen Evolution Reaction in Alkaline Solution: From Theory, Single Crystal Models, to Practical Electrocatalysts, Angew. Chem. Int. Ed. 57 (2018) 7568-7579.

[12] W. Li, Y. Liu, M. Wu, X. Feng, S.A.T. Redfern, Y. Shang, X. Yong, T. Feng, K. Wu, Z. Liu, B. Li, Z. Chen, J.S. Tse, S. Lu, B. Yang, Carbon-Quantum-Dots-Loaded Ruthenium Nanoparticles as an Efficient Electrocatalyst for Hydrogen Production in Alkaline Media, Adv. Mater. 30 (2018) e1800676.

[13] J. Zhu, L. Hu, P. Zhao, L.Y.S. Lee, K.Y. Wong, Recent Advances in Electrocatalytic Hydrogen Evolution Using Nanoparticles, Chem. Rev. 120 (2020) 851-918.

[14] L. Zhang, H. Jang, Y. Wang, Z. Li, W. Zhang, M.G. Kim, D. Yang, S. Liu, X. Liu, J. Cho, Exploring the Dominant Role of Atomic- and Nano-Ruthenium as Active Sites for Hydrogen Evolution Reaction in Both Acidic and Alkaline Media, Adv. Sci. 8 (2021) 2004516.

[15] J. Mao, C.T. He, J. Pei, W. Chen, D. He, Y. He, Z. Zhuang, C. Chen, Q. Peng, D. Wang, Y. Li, Accelerating water dissociation kinetics by isolating cobalt atoms into ruthenium lattice, Nat. Commun. 9 (2018) 4958.

[16] Y. Li, Y. Guo, S. Yang, Q. Li, S. Chen, B. Lu, H. Zou, X. Liu, X. Tong, H. Yang, Mesoporous RhRu Nanosponges with Enhanced Water Dissociation toward Efficient Alkaline Hydrogen Evolution, ACS Appl. Mater. Interfaces. 13 (2021) 5052-5060.

[17] X. Qin, L. Zhang, G.-L. Xu, S. Zhu, Q. Wang, M. Gu, X. Zhang, C. Sun, P.B. Balbuena, K. Amine, M. Shao, The Role of Ru in Improving the Activity of Pd toward Hydrogen Evolution and Oxidation Reactions in Alkaline Solutions, ACS Catal. 9 (2019) 9614-9621.

[18] J. Yu, Y. Dai, X. Wu, Z. Zhang, Q. He, C. Cheng, Z. Wu, Z. Shao, M. Ni, Ultrafine ruthenium-iridium alloy nanoparticles well-dispersed on N-rich carbon frameworks as efficient hydrogen-generation electrocatalysts, Chem. Eng. J. 417 (2021).

[19] J. Su, Y. Yang, G. Xia, J. Chen, P. Jiang, Q. Chen, Ruthenium-cobalt nanoalloys

encapsulated in nitrogen-doped graphene as active electrocatalysts for producing hydrogen in alkaline media, Nat. Commun. 8 (2017) 14969.

[20] C. Cai, K. Liu, Y. Zhu, P. Li, Q. Wang, B. Liu, S. Chen, H. Li, L. Zhu, H. Li, J. Fu, Y. Chen, E. Pensa, J. Hu, Y.R. Lu, T.S. Chan, E. Cortes, M. Liu, Optimizing Hydrogen Binding on Ru Sites with RuCo Alloy Nanosheets for Efficient Alkaline Hydrogen Evolution, Angew. Chem. Int. Ed. 61 (2022) e202113664.

[21] W. Li, Y. Zhao, Y. Liu, M. Sun, G.I.N. Waterhouse, B. Huang, K. Zhang, T. Zhang, S. Lu, Exploiting Ru-Induced Lattice Strain in CoRu Nanoalloys for Robust Bifunctional Hydrogen Production, Angew. Chem. Int. Ed. Engl. 60 (2021) 3290-3298.

[22] Q. Wu, M. Luo, J. Han, W. Peng, Y. Zhao, D. Chen, M. Peng, J. Liu, F.M.F. de Groot, Y. Tan, Identifying Electrocatalytic Sites of the Nanoporous Copper–Ruthenium Alloy for Hydrogen Evolution Reaction in Alkaline Electrolyte, ACS Energy Lett. 5 (2019) 192-199.

[23] K. Tu, D. Tranca, F. Rodriguez-Hernandez, K. Jiang, S. Huang, Q. Zheng, M.X. Chen, C. Lu, Y. Su, Z. Chen, H. Mao, C. Yang, J. Jiang, H.W. Liang, X. Zhuang, A Novel Heterostructure Based on RuMo Nanoalloys and N-doped Carbon as an Efficient Electrocatalyst for the Hydrogen Evolution Reaction, Adv. Mater. 32 (2020) 2005433.

[24] I.T. McCrum, M.T.M. Koper, The role of adsorbed hydroxide in hydrogen evolution reaction kinetics on modified platinum, Nat. Energy 5 (2020) 891-899.

[25] S. Zhu, X. Qin, F. Xiao, S. Yang, Y. Xu, Z. Tan, J. Li, J. Yan, Q. Chen, M. Chen, M. Shao, The role of ruthenium in improving the kinetics of hydrogen oxidation and evolution reactions of platinum, Nat. Catal. 4 (2021) 711-718.

[26] X. Wang, Y. Zhu, A. Vasileff, Y. Jiao, S. Chen, L. Song, B. Zheng, Y. Zheng, S.-Z. Qiao, Strain Effect in Bimetallic Electrocatalysts in the Hydrogen Evolution Reaction, ACS Energy Lett. 3 (2018) 1198-1204.

[27] D. Strmcnik, M. Uchimura, C. Wang, R. Subbaraman, N. Danilovic, D. van der Vliet, A.P. Paulikas, V.R. Stamenkovic, N.M. Markovic, Improving the hydrogen oxidation reaction rate by promotion of hydroxyl adsorption, Nat. Chem. 5 (2013)

300-306.

[28] S. Ye, F. Luo, T. Xu, P. Zhang, H. Shi, S. Qin, J. Wu, C. He, X. Ouyang, Q. Zhang, J. Liu, X. Sun, Boosting the alkaline hydrogen evolution of Ru nanoclusters anchored on B/N–doped graphene by accelerating water dissociation, Nano Energy 68 (2020) 104301.

[29] H. Li, M. Zhang, L. Yi, Y. Liu, K. Chen, P. Shao, Z. Wen, Ultrafine Ru nanoparticles confined in 3D nitrogen-doped porous carbon nanosheet networks for alkali-acid Zn-H_2 hybrid battery, Appl. Catal. B: Environ. 280 (2021) 119412.

[30] Z. Lin, B. Xiao, M. Huang, L. Yan, Z. Wang, Y. Huang, S. Shen, Q. Zhang, L. Gu, W. Zhong, Realizing Negatively Charged Metal Atoms through Controllable d-Electron Transfer in Ternary $Ir_{1-x}Rh_xSb$ Intermetallic Alloy for Hydrogen Evolution Reaction, Adv. Energy Mater. (2022) 2200855.

[31] M. Li, K. Duanmu, C. Wan, T. Cheng, L. Zhang, S. Dai, W. Chen, Z. Zhao, P. Li, H. Fei, Y. Zhu, R. Yu, J. Luo, K. Zang, Z. Lin, M. Ding, J. Huang, H. Sun, J. Guo, X. Pan, W.A. Goddard, P. Sautet, Y. Huang, X. Duan, Single-atom tailoring of platinum nanocatalysts for high-performance multifunctional electrocatalysis, Nat. Catal. 2 (2019) 495-503.

[32] B. Qiao, A. Wang, X. Yang, L.F. Allard, Z. Jiang, Y. Cui, J. Liu, J. Li, T. Zhang, Single-atom catalysis of CO oxidation using Pt1/FeO_x, Nat. Chem. 3 (2011) 634-641.

[33] Y. Sun, Z. Xue, Q. Liu, Y. Jia, Y. Li, K. Liu, Y. Lin, M. Liu, G. Li, C.Y. Su, Modulating electronic structure of metal-organic frameworks by introducing atomically dispersed Ru for efficient hydrogen evolution, Nat. Commun. 12 (2021) 1369.

[34] Z.W. Seh, J. Kibsgaard, C.F. Dickens, I. Chorkendorff, J.K. Norskov, T.F. Jaramillo, Combining theory and experiment in electrocatalysis: Insights into materials design, Science 355 (2017) 146.

[35] J. Mahmood, F. Li, S.M. Jung, M.S. Okyay, I. Ahmad, S.J. Kim, N. Park, H.Y. Jeong, J.B. Baek, An efficient and pH-universal ruthenium-based catalyst for the hydrogen evolution reaction, Nat. Nanotechnol. 12 (2017) 441-446.

[36] D.H. Kweon, M.S. Okyay, S.J. Kim, J.P. Jeon, H.J. Noh, N. Park, J. Mahmood,

J.B. Baek, Ruthenium anchored on carbon nanotube electrocatalyst for hydrogen production with enhanced Faradaic efficiency, Nat. Commun. 11 (2020) 1278.

[37] Q. Ju, R. Ma, Y. Pei, B. Guo, Z. Li, Q. Liu, T. Thomas, M. Yang, G.J. Hutchings, J. Wang, Ruthenium Triazine Composite: A Good Match for Increasing Hydrogen Evolution Activity through Contact Electrification, Adv. Energy Mater. 10 (2020) 2000067.

[38] Y. Liu, Y. Yang, Z. Peng, Z. Liu, Z. Chen, L. Shang, S. Lu, T. Zhang, Self-crosslinking carbon dots loaded ruthenium dots as an efficient and super-stable hydrogen production electrocatalyst at all pH values, Nano Energy 65 (2019).

[39] Y.Y. Zhang, N. Zhang, P. Peng, R. Wang, Y. Jin, Y.K. Lv, X. Wang, W. Wei, S.Q. Zang, Uniformly Dispersed Ru Nanoparticles Constructed by In Situ Confined Polymerization of Ionic Liquids for the Electrocatalytic Hydrogen Evolution Reaction, Small Methods 5 (2021) 2100505.

[40] Z. Wang, Y. Zhang, E.C. Neyts, X. Cao, X. Zhang, B.W.L. Jang, C.-j. Liu, Catalyst Preparation with Plasmas: How Does It Work? ACS Catal. 8 (2018) 2093-2110.

[41] W. Tang, J. Li, J. Zheng, W. Chu, N. Wang, Atomically dispersed metal sites stabilized on a nitrogen doped carbon carrier via N_2 glow-discharge plasma, Chem. Commun. 56 (2020) 9198-9201.

[42] J. Li, Y. Zhou, W. Tang, J. Zheng, X. Gao, N. Wang, X. Chen, M. Wei, X. Xiao, W. Chu, Cold-plasma technique enabled supported Pt single atoms with tunable coordination for hydrogen evolution reaction, Appl. Catal. B: Environ. 285 (2021) 119861.

[43] J. Hong, W. Chu, P.A. Chernavskii, A.Y. Khodakov, Cobalt species and cobalt-support interaction in glow discharge plasma-assisted Fischer–Tropsch catalysts, J. Catal. 273 (2010) 9-17.

[44] J. Hong, J. Du, B. Wang, Y. Zhang, C. Liu, H. Xiong, F. Sun, S. Chen, J. Li, Plasma-Assisted Preparation of Highly Dispersed Cobalt Catalysts for Enhanced Fischer–Tropsch Synthesis Performance, ACS Catal. 8 (2018) 6177-6185.

[45] C. Hu, E. Song, M. Wang, W. Chen, F. Huang, Z. Feng, J. Liu, J. Wang, Partial-

Single-Atom, Partial-Nanoparticle Composites Enhance Water Dissociation for Hydrogen Evolution, Adv. Sci. 8 (2021) 2001881.

[46] C. Fan, X. Jiang, J. Chen, X. Wang, S. Qian, C. Zhao, L. Ding, D. Sun, Y. Tang, Low-Load Pt Nanoclusters Anchored on Graphene Hollow Spheres for Efficient Hydrogen Evolution, Small Struct. 2 (2020) 2000017.

[47] B. Pang, X. Liu, T. Liu, T. Chen, X. Shen, W. Zhang, S. Wang, T. Liu, D. Liu, T. Ding, Z. Liao, Y. Li, C. Liang, T. Yao, Laser-assisted high-performance PtRu alloy for pH-universal hydrogen evolution, Energy Environ. Sci. 15 (2022) 102-108.

[48] S. Fang, X. Zhu, X. Liu, J. Gu, W. Liu, D. Wang, W. Zhang, Y. Lin, J. Lu, S. Wei, Y. Li, T. Yao, Uncovering near-free platinum single-atom dynamics during electrochemical hydrogen evolution reaction, Nat. Commun. 11 (2020) 1029.

[49] C.H. Chen, D. Wu, Z. Li, R. Zhang, C.G. Kuai, X.R. Zhao, C.K. Dong, S.Z. Qiao, H. Liu, X.W. Du, Ruthenium-Based Single-Atom Alloy with High Electrocatalytic Activity for Hydrogen Evolution, Adv. Energy Mater. 9 (2019) 1803913.

[50] G. Meng, H. Tian, L. Peng, Z. Ma, Y. Chen, C. Chen, Z. Chang, X. Cui, J. Shi, Ru to W electron donation for boosted HER from acidic to alkaline on Ru/WNO sponges, Nano Energy 80 (2021) 105531.

[51] Z.L. Wang, K. Sun, J. Henzie, X. Hao, C. Li, T. Takei, Y.M. Kang, Y. Yamauchi, Spatially Confined Assembly of Monodisperse Ruthenium Nanoclusters in a Hierarchically Ordered Carbon Electrode for Efficient Hydrogen Evolution, Angew. Chem. Int. Ed. Engl. 57 (2018) 5848-5852.

[52] Y. Li, J. Abbott, Y. Sun, J. Sun, Y. Du, X. Han, G. Wu, P. Xu, Ru nanoassembly catalysts for hydrogen evolution and oxidation reactions in electrolytes at various pH values, Appl. Catal. B 258 (2019) 117952.

[53] P. Jiang, Y. Yang, R. Shi, G. Xia, J. Chen, J. Su, Q. Chen, Pt-like electrocatalytic behavior of Ru–MoO_2 nanocomposites for the hydrogen evolution reaction, J. Mater. Chem. A 5 (2017) 5475-5485.

[54] M. Li, H. Wang, W. Zhu, W. Li, C. Wang, X. Lu, RuNi Nanoparticles Embedded in N-Doped Carbon Nanofibers as a Robust Bifunctional Catalyst for Efficient

Overall Water Splitting, Adv. Sci. 7 (2020) 1901833.

[55] B. Tang, X. Yang, Z. Kang, L. Feng, Crystallized RuTe2 as unexpected bifunctional catalyst for overall water splitting, Appl. Catal. B: Environ. 278 (2020) 119281.

[56] E.R. Hamo, R.K. Singh, J.C. Douglin, S. Chen, M.B. Hassine, E. Carbo-Argibay, S. Lu, H. Wang, P.J. Ferreira, B.A. Rosen, D.R. Dekel, Carbide-Supported PtRu Catalysts for Hydrogen Oxidation Reaction in Alkaline Electrolyte, ACS Catal. 11 (2021) 932-947.

[57] P. Li, G. Zhao, P. Cui, N. Cheng, M. Lao, X. Xu, S.X. Dou, W. Sun, Nickel single atom-decorated carbon nanosheets as multifunctional electrocatalyst supports toward efficient alkaline hydrogen evolution, Nano Energy 83 (2021) 105850.

[58] J. Ohyama, D. Kumada, A. Satsuma, Improved hydrogen oxidation reaction under alkaline conditions by ruthenium–iridium alloyed nanoparticles, J. Mater. Chem. A 4 (2016) 15980-15985.

[59] Y. Liu, X. Li, Q. Zhang, W. Li, Y. Xie, H. Liu, L. Shang, Z. Liu, Z. Chen, L. Gu, Z. Tang, T. Zhang, S. Lu, A General Route to Prepare Low-Ruthenium-Content Bimetallic Electrocatalysts for pH-Universal Hydrogen Evolution Reaction by Using Carbon Quantum Dots, Angew. Chem. Int. Ed. Engl. 59 (2020) 1718-1726.

[60] M. Luo, J. Cai, J. Zou, Z. Jiang, G. Wang, X. Kang, Promoted alkaline hydrogen evolution by an N-doped Pt–Ru single atom alloy, J. Mater. Chem. A 9 (2021) 14941-14947.

Graphic abstract:

Atomically dispersed Pt on ultrafine Ru nanoclusters (~1.46 nm) loaded by the commercial acetylene black support is fabricated by a facile one-step cold-plasma technique. The Pt single atoms on Ru nanoclusters electrocatalyst ($Pt_{0.47}$-Ru/Acet) with 0.47 wt% content of Pt exhibits an excellent HER activity in all pH, achieving ultralow overpotential of only 17, 28, and 8 mV at 10 $mA \cdot cm^{-2}$ in 1 M KOH, 0.5 M H_2SO_4, and 1 M PBS, respectively.

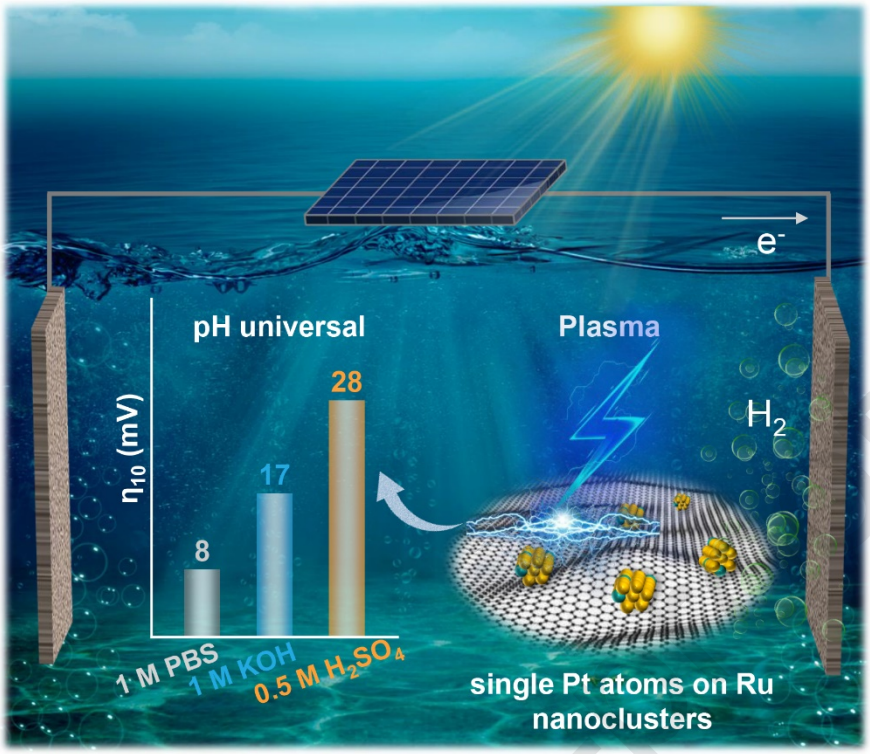

Highlights:

- Cold plasma enables ultrafine Ru nanoclusters compared with calcination method.
- Atomically dispersed Pt-modified Ru is fabricated by a cold-plasma technique.
- $Pt_{0.47}$-Ru/Acet displays excellent pH-universal HER activity.
- DFT calculations reveal the mechanism of Pt enhancement in alkaline HER.
- Both anode and cathode use $Pt_{0.47}$-Ru/Acet in solar-driving water splitting.

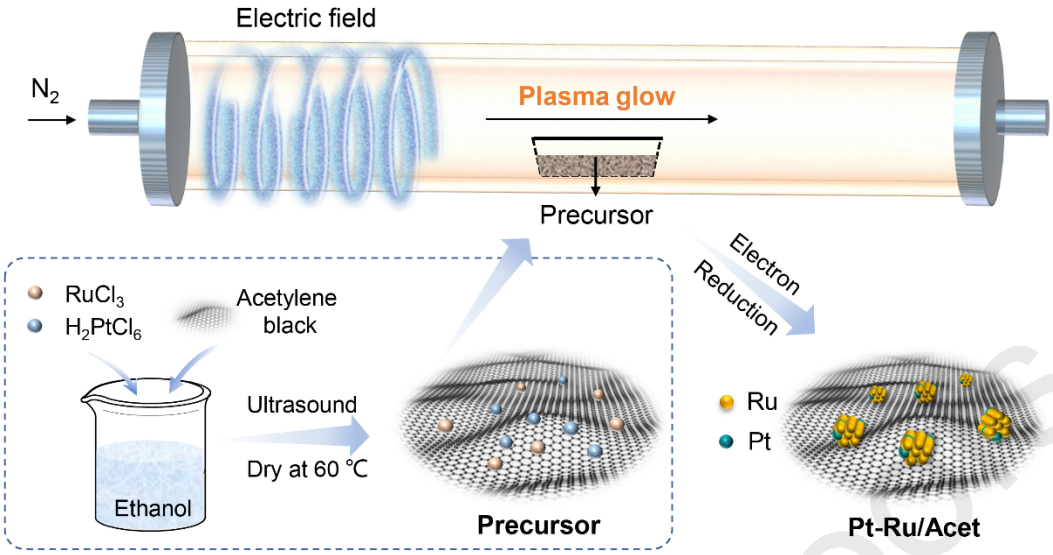

Scheme 1. Schematic illustration of the synthesis of $Pt_{0.47}$-Ru/Acet catalyst by electron reduction of plasma.

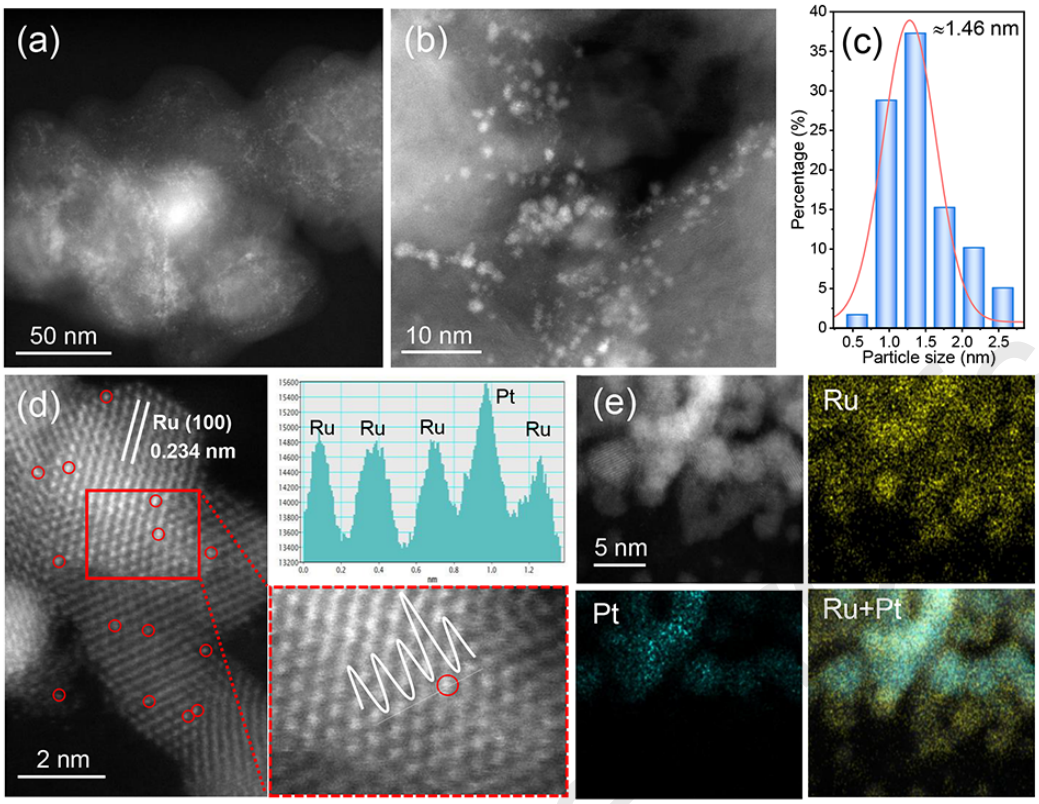

Figure 1. **The structural characterization on $Pt_{0.47}$-Ru/Acet.** (a, b) The TEM images of $Pt_{0.47}$-Ru/Acet. (c) the corresponding nanoparticle size distribution of $Pt_{0.47}$-Ru/Acet.(d) Atomic-resolution HAADF-STEM image. Magnified image in red box, Pt atom was marked with red circles. (e) EDS elemental maps of Ru and Pt.

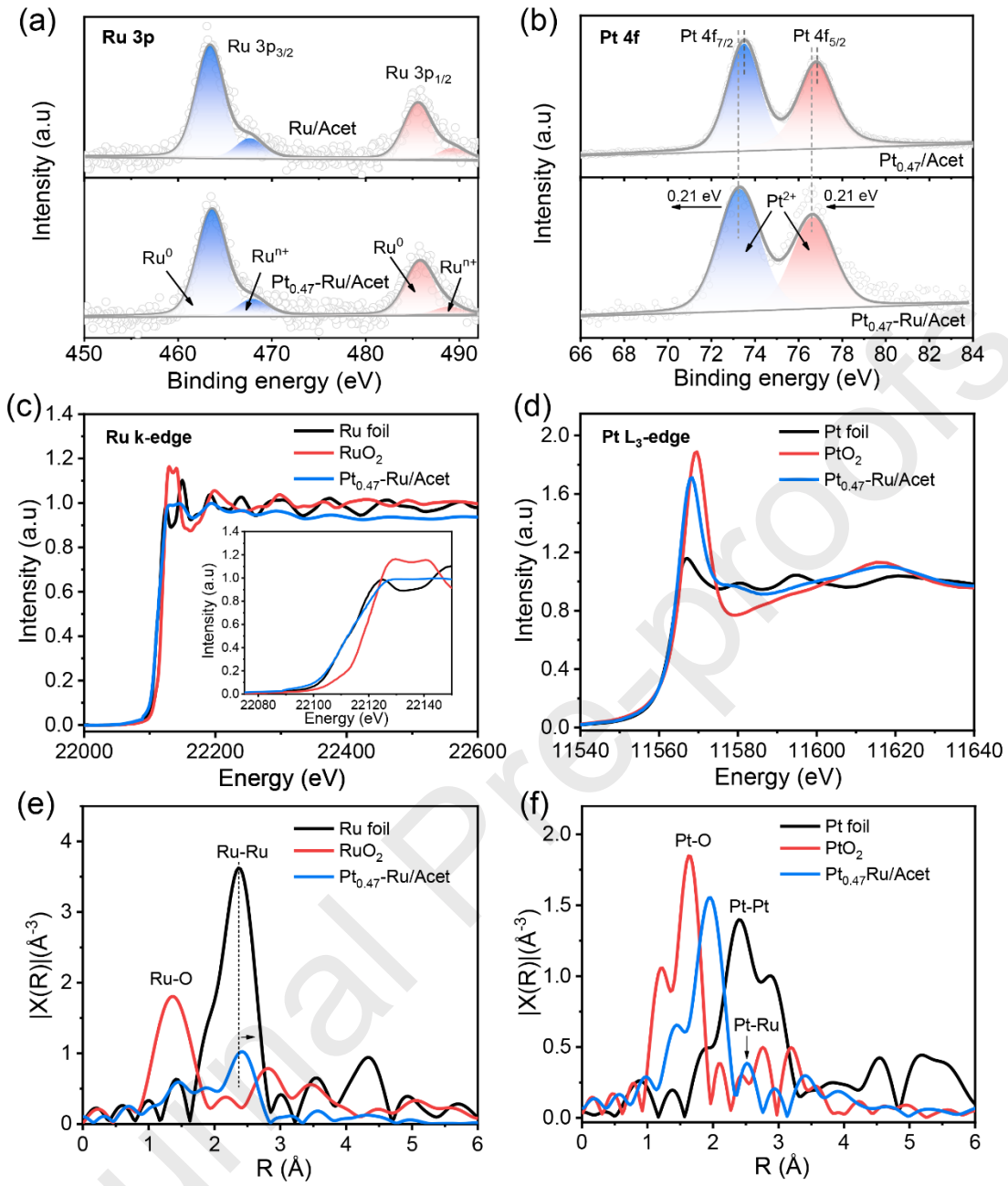

Figure 2. High-resolution XPS spectra of the as-prepared samples for (a) Ru 3p and (b) Pt 4f. (c) Ru K-edge XANES spectra of Ru foil, RuO_2, and $Pt_{0.47}$-Ru/Acet. (d) Pt L_3-edge XANES spectra of Pt foil, PtO_2, and $Pt_{0.47}$-Ru/Acet. (e) Fourier transforms of EXAFS spectra of Ru foil, RuO_2, and $Pt_{0.47}$-Ru/Acet. (f) Fourier transforms of EXAFS spectra of Pt foil, PtO_2, and $Pt_{0.47}$-Ru/Acet.

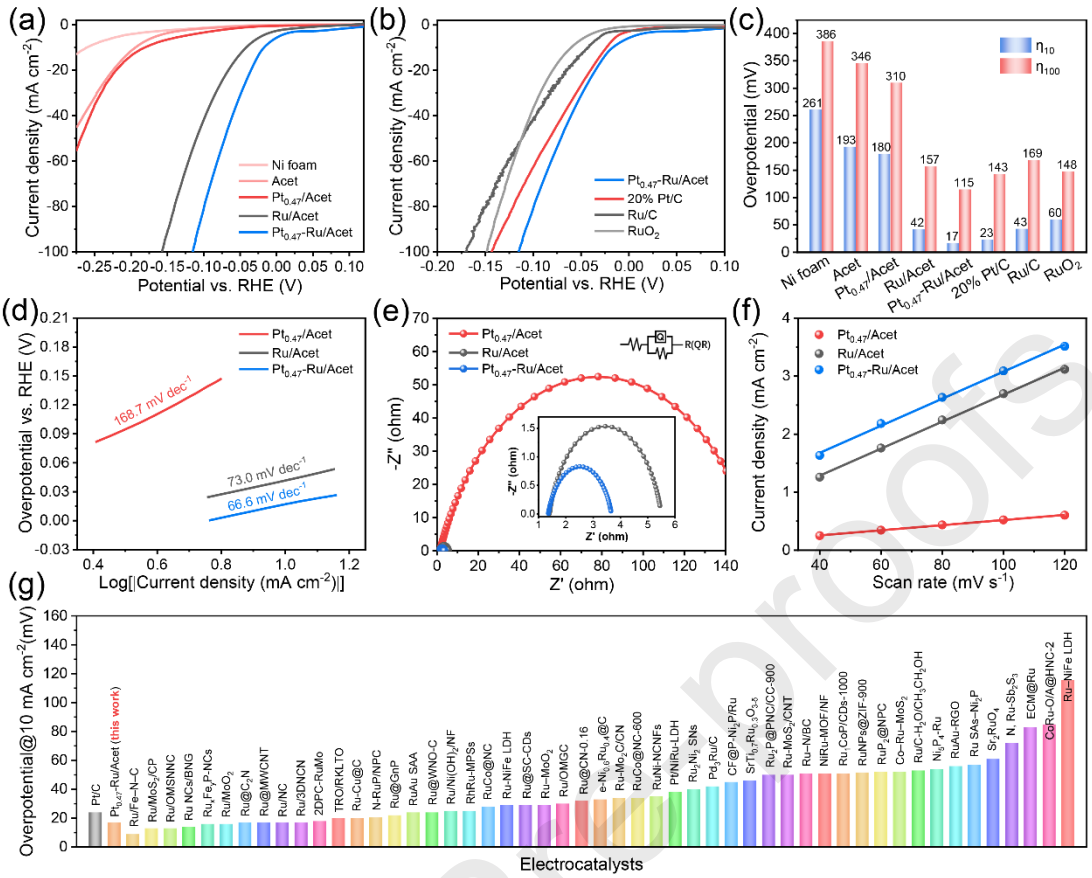

Figure 3. HER performance of the as-prepared catalysts in 1 M KOH solution. (a) and (b) LSV polarization curves (iR corrected) of Ni foam, Acet, Ru/Acet, $Pt_{0.47}$-Ru /Acet, commercial 20 wt% Pt/C, 5 wt% Ru/C, and RuO_2 at a scan rate of 10 mV s^{-1}. (c) Corresponding overpotentials at 10 mA cm^{-2} and 100 mA cm^{-2}. (d) Tafel slopes from the polarization curves. (e) EIS spectra of different electrocatalysts. (f) Corresponding electrochemical double layer capacitances. (g) Comparison of the HER activity for Ru-based electrocatalysts with other reported in 1 M KOH solution.

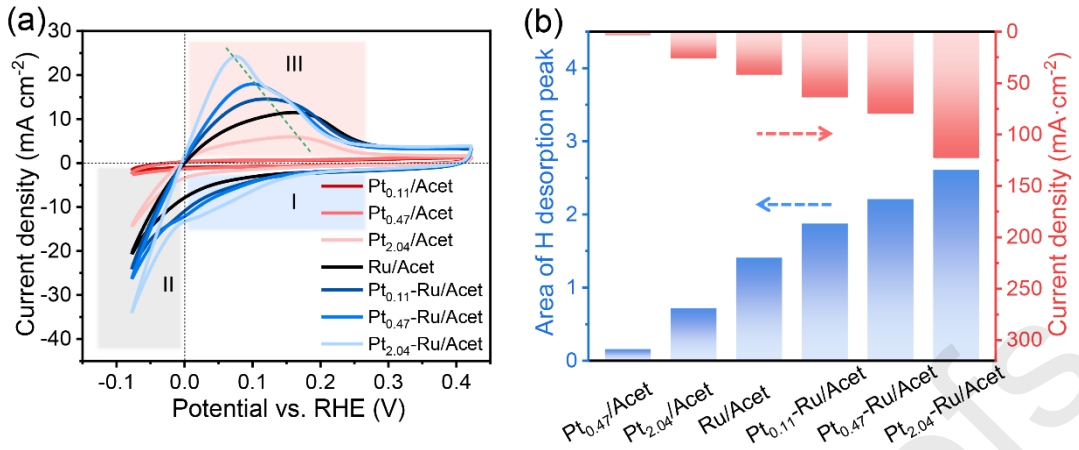

Figure 4. (a) The stabilized CV curves for $Pt_{0.11}$/Acet, $Pt_{0.47}$/Acet, Ru/Acet, $Pt_{2.04}$/Acet, $Pt_{0.11}$-Ru/Acet, $Pt_{0.47}$-Ru/Acet and $Pt_{2.04}$-Ru/Acet catalysts in 1 M KOH solution. (b) Corresponding the area of H desorption peak and current density at η_{100}.

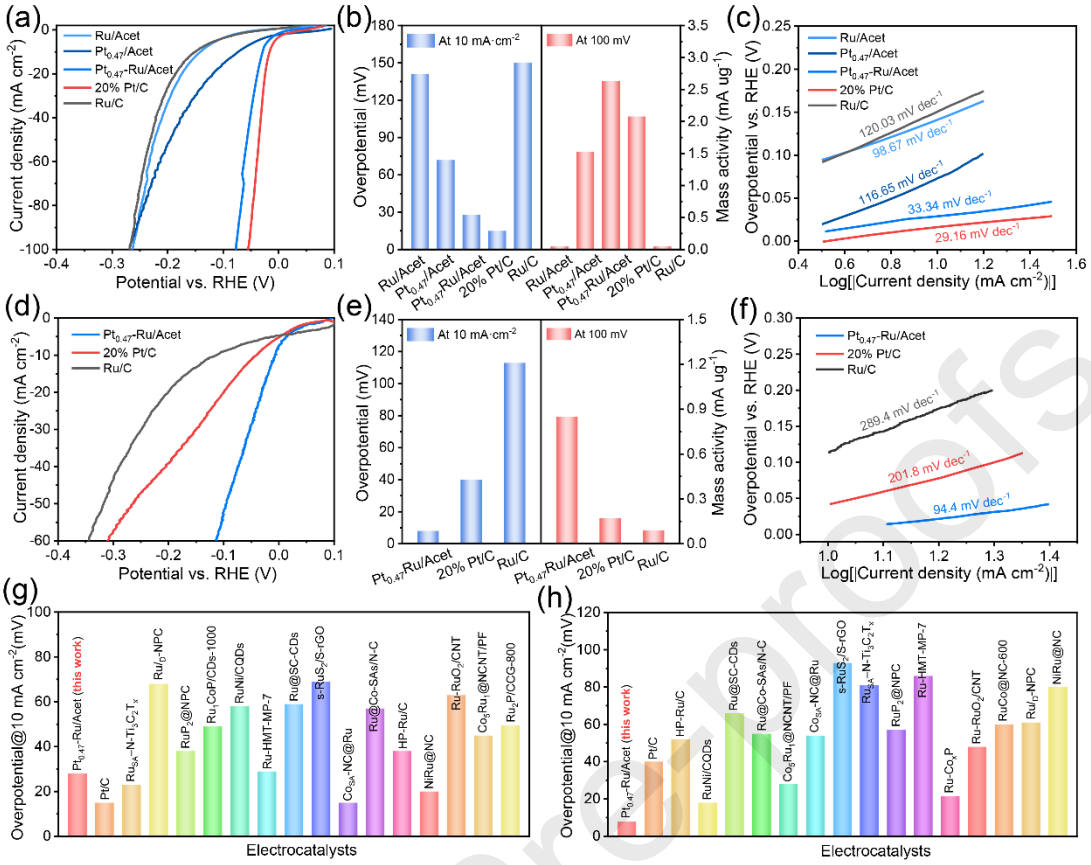

Figure 5. HER performance of the as-prepared catalysts in 0.5 M H_2SO_4 and 1M PBS solution. LSV polarization curves (iR corrected) of $Pt_{0.47}$-Ru/Acet, commercial 20 wt% Pt/C, 5 wt% Ru/C and RuO_2 in 0.5 M H_2SO_4 (a) and 1M PBS (d). Corresponding overpotentials and mass activity in 0.5 M H_2SO_4 (b) and 1M PBS (e). Tafel slopes from the polarization curves (c) and (f). Comparison of the HER activity for Ru-based electrocatalysts with other reported in 0.5 M H_2SO_4 (g) and 1M PBS (h).

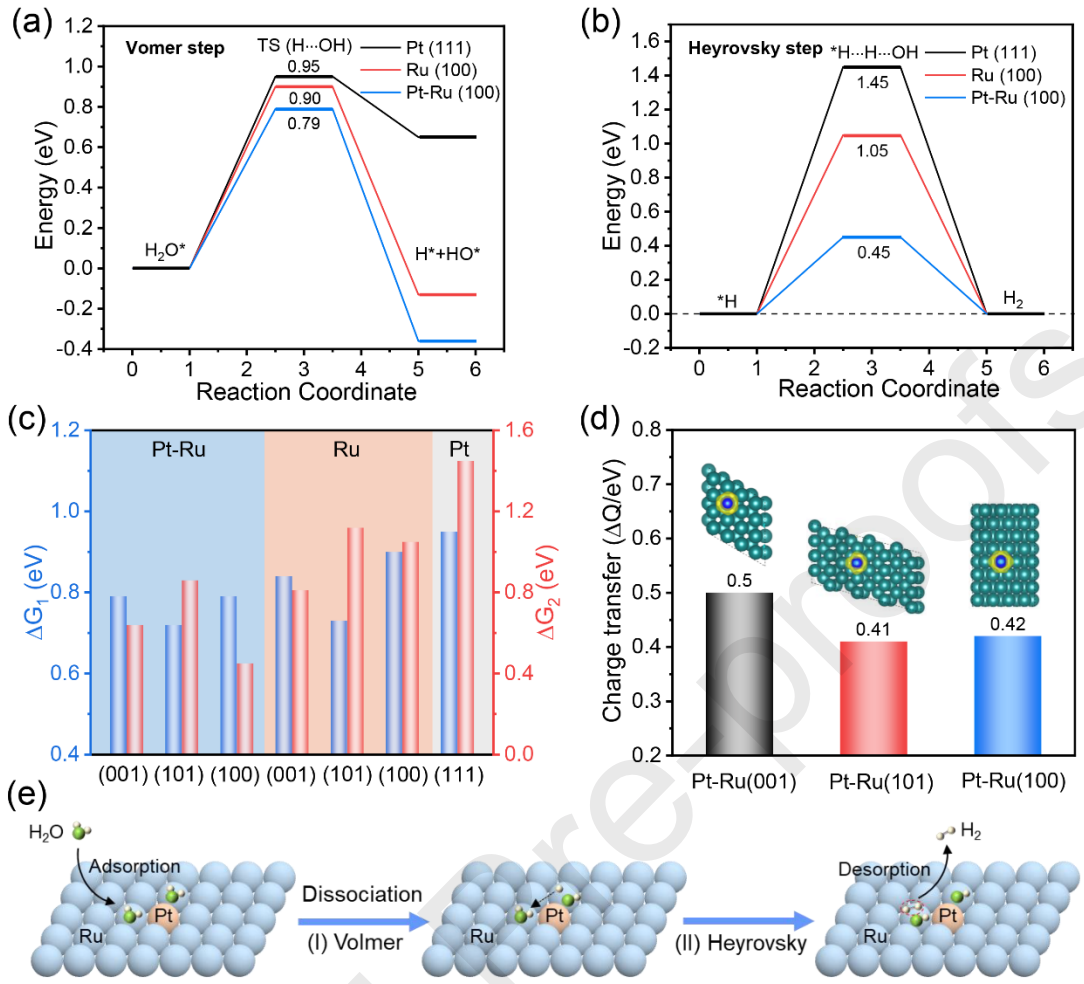

Figure 6. DFT calculations. Energy diagrams of water dissociation (a) and Heyrovsky step (b) for Pt-Ru (001), Ru (100), and Pt (111), respectively. (c) The calculated energy diagrams for the Volmer step (ΔG_1) and Heyrovsky step (ΔG_2) on the Pt-Ru, Ru and Pt over various exposed surfaces (001), (101), (100), and (111). (d) The value of charge transfer from Ru to Pt on Pt-Ru (001), Pt-Ru (101) and Pt-Ru (100) surface. (e) Schematic illustration of the alkaline HER mechanism on Pt-Ru/Acet.

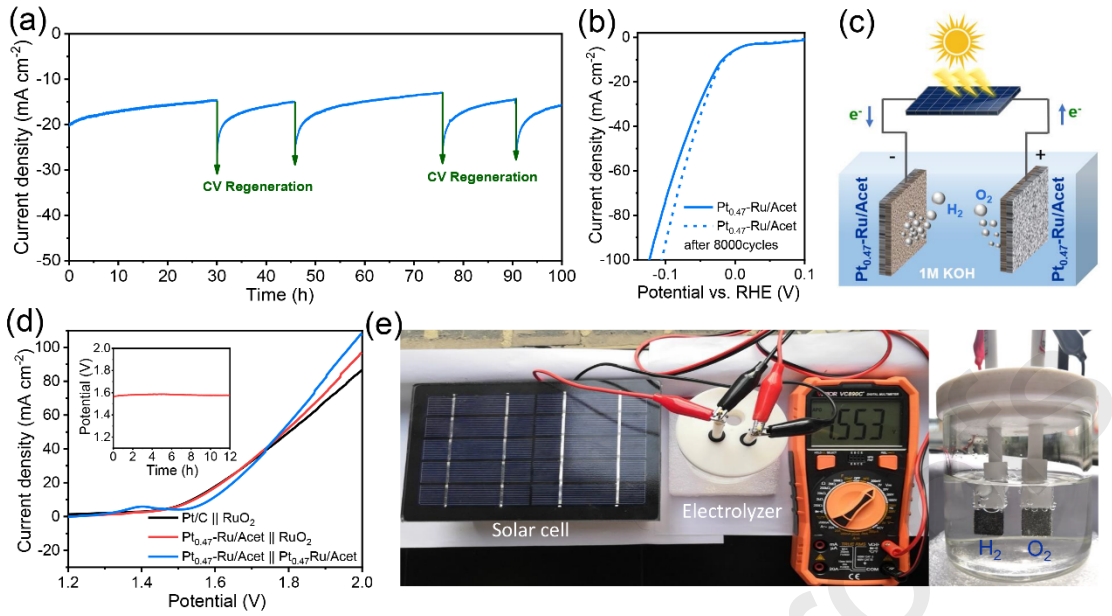

Figure 7. Stability and overall water splitting. (a) i-t curves of $Pt_{0.47}$-Ru/Acet at an overpotential of 20 mA cm^{-2}. (b) LSV curves of $Pt_{0.47}$-Ru/Acet before and after 8000 CV cycles with graphite rod as the counter electrode. (c) Schematic diagram of the photovoltaic-driven overall water splitting. (d) LSV polarization curves of $Pt_{0.47}$-Ru/Acet || $Pt_{0.47}$-Ru/Acet, $Pt_{0.47}$-Ru/Acet || RuO_2, Pt/C || RuO_2 electrolyzer for overall water splitting in 1M KOH without iR compensation. Inset: chronopotentiometry curve of $Pt_{0.47}$-Ru/Acet || RuO_2 for 12h. (e) photograph of the integrated water splitting device with solar panel assisted and the magnified image of electrolyzer.

Declaration of Competing Interest

The authors declare that they have no known competing financial interests or personal relationships that could have appeared to influence the work reported in this paper.